

Analysis of nose landing gear noise comparing numerical computations, prediction models and flyover and wind-tunnel measurements

Merino-Martinez, Roberto; Neri, Eleonora; Snellen, Mirjam; Kennedy, John; Simons, Dick G.; Bennett, Gareth J.

DOI

[10.2514/6.2018-3299](https://doi.org/10.2514/6.2018-3299)

Publication date

2018

Document Version

Accepted author manuscript

Published in

2018 AIAA/CEAS Aeroacoustics Conference

Citation (APA)

Merino-Martinez, R., Neri, E., Snellen, M., Kennedy, J., Simons, D. G., & Bennett, G. J. (2018). Analysis of nose landing gear noise comparing numerical computations, prediction models and flyover and wind-tunnel measurements. In *2018 AIAA/CEAS Aeroacoustics Conference [AIAA 2018-3299]* American Institute of Aeronautics and Astronautics Inc. (AIAA). <https://doi.org/10.2514/6.2018-3299>

Important note

To cite this publication, please use the final published version (if applicable).
Please check the document version above.

Copyright

Other than for strictly personal use, it is not permitted to download, forward or distribute the text or part of it, without the consent of the author(s) and/or copyright holder(s), unless the work is under an open content license such as Creative Commons.

Takedown policy

Please contact us and provide details if you believe this document breaches copyrights.
We will remove access to the work immediately and investigate your claim.

Analysis of nose landing gear noise comparing numerical computations, prediction models and flyover and wind-tunnel measurements

Roberto Merino-Martínez^{*1}, Eleonora Neri^{†2}, Mirjam Snellen^{‡1}, John Kennedy^{§2}, Dick G. Simons^{¶1}, and Gareth J. Bennett^{||2}

¹*Delft University of Technology, 2629 HS Delft, the Netherlands*

²*Trinity College Dublin, Ireland*

The noise emissions of a full-scale nose landing gear, measured in a wind tunnel and obtained from computational simulations, are compared with those of three regional aircraft types recorded in flyover measurements. The results from these three approaches are also compared with the predictions of two airframe noise models (Fink and Guo). The geometries of the nose landing gears in all cases were similar. Microphone arrays and acoustic imaging algorithms were employed to estimate the sound emissions of the nose landing gears. A good agreement was found between the overall trends of the frequency spectra in all cases. Moreover, the expected 6th power law with the flow velocity was confirmed. On the other hand, strong tonal peaks (at around 2200 Hz) were only found for the flyover tests and computational simulations and are not present in typical noise prediction models. As the frequencies of the tones did not depend on the flow velocity, they are likely to be caused by cavities found in structural components of the nose landing gear. Removing these tones would cause overall noise reductions up to 2 dB in the frequency range examined. The noise emissions in the side direction did not present tonal peaks. The acoustic source maps showed that the dominant noise sources were located in the middle of the wheel axle, followed by the main strut and the bay doors. It is, therefore, recommended to further investigate this phenomenon, to include cavity-noise estimations in the current noise prediction models, and to eliminate such cavities where possible with the use of cavity caps, for example.

I. Introduction

NOISE emissions from flying aircraft are becoming an increasingly important issue and a severe source of annoyance for the population around airports. Technological advances over the last decades, such as high-bypass turbofan engines and acoustic liners [1], have achieved considerable reductions in engine noise levels. Thus, airframe noise (generated by the interaction between the aerodynamic surfaces and the surrounding unsteady turbulent flow [2]) can present comparable sound pressure levels (SPL or L_p) as engine noise during the approach stage because the engines normally operate low thrust settings, and it may constitute a lower bound to aircraft noise in the future [3, 4]. Governmental organizations, such as ACARE [5] (Advisory Council for Aviation Research and Innovation in Europe) and projects such as Flight Path

^{*}PhD candidate, Aircraft Noise & Climate Effects section, Faculty of Aerospace Engineering, Kluyverweg 1. AIAA Student Member. E-mail: r.merinomartinez@tudelft.nl

[†]PhD candidate, Department of Mechanical and Manufacturing Engineering. AIAA Student Member. E-mail: eneri@tcd.ie

[‡]Associate professor, Aircraft Noise & Climate Effects section, Faculty of Aerospace Engineering, Kluyverweg 1. E-mail: m.snellen@tudelft.nl

[§]Assistant Professor, Department of Mechanical and Manufacturing Engineering. E-mail: kennedj@tcd.ie

[¶]Full professor, Aircraft Noise & Climate Effects section, Faculty of Aerospace Engineering, Kluyverweg 1. E-mail: d.g.simons@tudelft.nl

^{||}Associate Professor, Department of Mechanical and Manufacturing Engineering. AIAA Senior Member. E-mail: gareth.bennett@tcd.ie

2050 [6] aim at a 65% reduction of the perceived aircraft noise levels by 2050 compared to the levels in 2000 (equivalent to a reduction of 15 dB per operation).

Within this framework, the European Clean Sky funded project ALLEGRA (Advanced Low Noise Landing (Main and Nose) Gear for Regional Aircraft) was developed to assess the performance of low-noise technologies applied to a full-scale nose landing gear (NLG) model [7, 8] and a half-scale main landing gear (MLG) model [9] of a high-wing regional aircraft. ALLEGRA consisted of a consortium of universities (Trinity College Dublin and KTH), an aeroacoustic wind-tunnel company (Pininfarina SPA), and European SME manufacturing and design partners (Eurotech and Teknosud) supported by a leading landing gear manufacturer (Magnaghi Aeronautica).

The main source of airframe noise for commercial aircraft is the landing gear (LG) system [4, 10], which can generate approximately 30% of the whole aircraft noise emissions [11, 12]. The LG system typically consists of complicated structures of bluff bodies (struts, links, wheels, tires, fairings, etc.) of considerably different sizes, which are normally not optimized acoustically [3]. The sound generation mechanisms for LG systems are usually very complex and depend on the specific geometry and configuration of the LG. A typical sound signal from a LG system is a combination of broadband noise, mainly caused by the interaction of the LG with the turbulent flow, and tonal noise, generated by flow in cavities [3, 13, 14] and Aeolian tones due to flow separation and vortex shedding [15, 16]. The tone frequency due to a cavity mainly depends on the cavity geometry itself [13], whereas for Aeolian tones, it also depends on the flow velocity [16].

The noise emissions of the whole LG system are due to the combination of the contributions of the NLG and the MLG systems. Even though the MLG structure is typically larger and more complicated than the NLG (i.e., it is expected to be noisier), the flow velocity impinging the MLG system is approximately 20% lower than that of the NLG because of the recirculation of the flow underneath the wings [17]. Therefore, due to the strong dependence between the LG noise levels and the flow velocity [18], both LG systems usually emit comparable noise levels [19]. The object of study of this paper is the NLG system of regional aircraft, which represent a considerable share of the total flights in Europe (about 30% of the flights recorded in the campaign used in [20]).

There are several approaches to study LG noise. The methods employed in this paper are briefly described below, as well as their benefits and limitations:

1. **Wind-tunnel measurements** [7–9, 15, 21] offer relatively controlled flow conditions, but they require the LG model being tested to have a high level of geometric detail to represent the small-scale sound generating mechanisms [4, 10]. Moreover, it is difficult to replicate the exact conditions present around a flying aircraft, such as the Reynolds number or installation effects [22]. This approach also lacks the important feature of the relative motion between source and receiver [3]. According to Dobrzynski [4], noise prediction models based solely on wind-tunnel tests featuring scale models are prone to underestimate airframe noise levels compared to full-scale flight tests. In this paper, wind tunnel measurements [20] of the full-scale NLG model within the ALLEGRA project are considered.
2. **Flyover measurements** [10, 19, 20, 23] with aircraft under operational conditions present different challenges, such as the inability to control the aircraft position, larger distances between the sound source and the observer, and less-controlled flow and atmospheric characteristics, but they fully represent the actual conditions experienced in reality [24–26], such as crosswind. Hence, a comparison between the results of both experiments is of great interest [16]. Flyover field measurements under operational conditions recorded in Amsterdam Airport Schiphol [20] are employed in this study. Three different regional aircraft types (all equipped with turbofan engines) are selected for this paper.
3. **Computational simulations** [27–29] of a detailed LG geometry can be very time-consuming due to its complex structure. On the other hand, extensive wind-tunnel or flyover test campaigns usually have a large economic cost, limiting the amount of configurations available to study. In practice, for numerical simulations, the geometry of the LG is normally simplified to some extent where the computational cost is acceptable, such as the realistic NLG geometry from the ALLEGRA project [27–29] or the more simplified LAGooN geometry from ONERA [30]. One advantage of computational simulations is that they allow for non-intrusive measurements in directions that are impossible to investigate in experiments (such as upwind of the model) and that the acoustic data are usually *cleaner* than those recorded in experiments, allowing for shorter recording times. For this research, the computational simulations on the ALLEGRA NLG geometry performed by Bouchouireb et al. [27] are used for comparison.

4. **Noise prediction models** relying on empirical data or semi-empirical estimations, such as Fink’s [18] and Guo’s [31–33] methods, provide one-third-octave-band noise spectra estimations for different directivity angles for simplified LG geometries. They require some geometrical parameters as input, but they normally do not consider parasitic noise sources, such as cavities [19, 20]. Previous studies [19, 32, 34] showed that considerable differences exist between experimental measurements and the model predictions for LG noise. In addition, by their very nature, semi-empirical methods have a limited reliability in predicting the impact of noise reduction devices [27]. The noise prediction methods of Fink [18] and Guo [31–33] were applied to the ALLEGRA NLG geometry.

For aeroacoustic measurements, it is common to employ phased microphone arrays and acoustic imaging techniques for estimating the locations and strengths of the sound sources [8, 35–38] and isolate their contributions. These devices require short measurement times, allowing for relatively cheap and fast experiments [39]. The application of this approach to simulated data is, however, relatively new, yet promising and in intense development [27, 40].

For this research, both sets of experimental measurements and the computational simulations employ phased microphone arrays (a virtual array in the computational case) to separate the sound signal emitted at the NLG position. The performance of both noise prediction models will be assessed with respect to the experimental and numerical results.

The paper is structured as follows: Section II explains the experimental setups for the wind-tunnel and flyover measurements and the numerical setup and computational domain for the simulated case. Details about the NLG geometries considered are also included. The acoustic imaging techniques employed are summarized in Sec. III. Brief descriptions of Fink’s and Guo’s noise prediction models are provided in Sec. IV. The results obtained and the comparison between approaches are presented in Sec. V and Sec. VI gathers the most important conclusions.

II. Experimental and numerical setups

II.A. Wind-tunnel measurements

The NLG model used in the ALLEGRA project was full-scale, including a full representation of the NLG details and associated structures (e.g., bay cavity, bay doors, belly fuselage and hydraulic dressings). The LG geometry was obtained from an advanced regional turboprop aircraft design.

The experiments were performed in the Pininfarina open-jet, semi-cylindrical wind-tunnel facility in Turin, Italy, which has a test section of 8 m (length) \times 9.60 m (width) \times 4.20 m (height). The facility contains a low-noise, high-speed fan-driven system of 13 fans, which provides flow velocities up to 72.2 m/s and presents a background noise level of 68 dBA at 27.8 m/s. The background noise for the ALLEGRA NLG tests was considered as a combination of the wind-tunnel noise and the noise produced by the fuselage belly itself. Both are mostly low frequency noise sources (below 100 Hz), outside of the frequency range of interest. The flow velocity produced by the wind tunnel is very uniform, since it varies by only 0.5% over the test area. The turbulence intensity level had a value of 0.3% in these experiments.

Figure 1 depicts the relative position of the NLG model in the wind tunnel, as well as the coordinate system employed, where the xz plane is the symmetry plane of the test model, the yz plane corresponds to the wind-tunnel nozzle exit and the origin is situated in the floor of the testing platform (xy plane). The NLG complete model, with the fuselage belly and bay cavities, was placed in the wind tunnel so that the distance between the wind-tunnel nozzle and the NLG wheel axis was 2.8 m. Therefore, the coordinates of the middle point of the wheel axis were:

$$x = 2.8 \text{ m}; y = 0 \text{ m}; z = 2.175 \text{ m}.$$

Figure 2 shows a picture of the model inside the wind tunnel. Figure 3 presents the overall dimensions of the wind-tunnel test model.

The wind-tunnel model had a fixed, built-in angle of attack of 4° . Each model configuration was tested at a variety of flow speeds and yaw settings, allowing the analysis of conditions equivalent to landing with crosswind. For this paper, only the yaw angle of 0° (no crosswind) was considered. Flow velocities of 40, 50, 60 and 65 m/s were employed for the experiment, i.e., a maximum Mach number of about 0.19.

Four different planar microphone arrays were installed in the top, side and front of the wind tunnel. For the present study, only the data from two arrays were used:

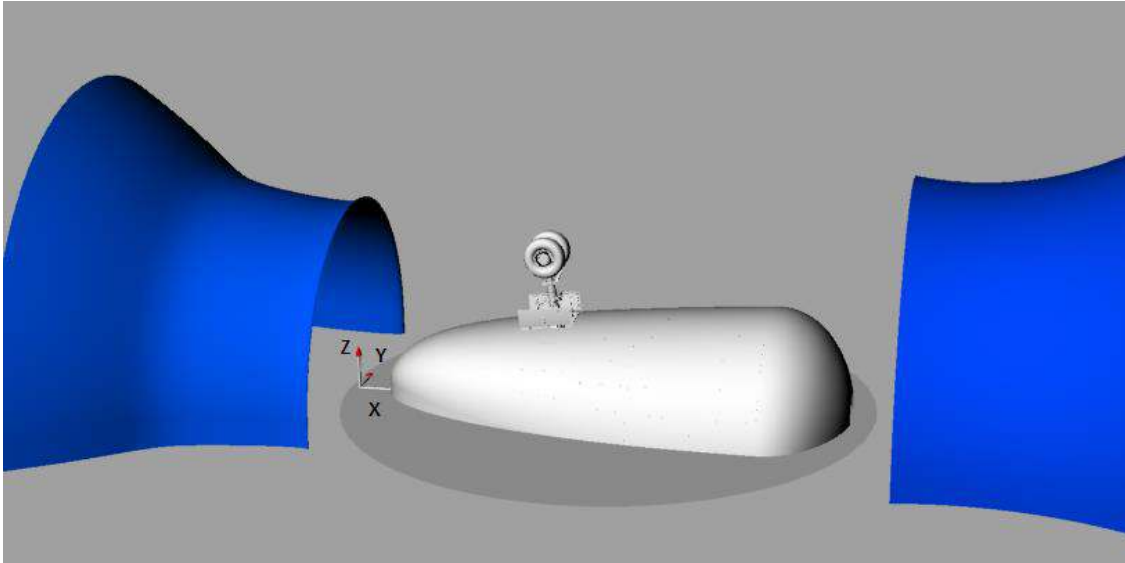


Figure 1: Model and coordinate system inside the Pininfarina wind tunnel [41].



Figure 2: ALLEGRA NLG model inside the wind tunnel with the top array visible [41].

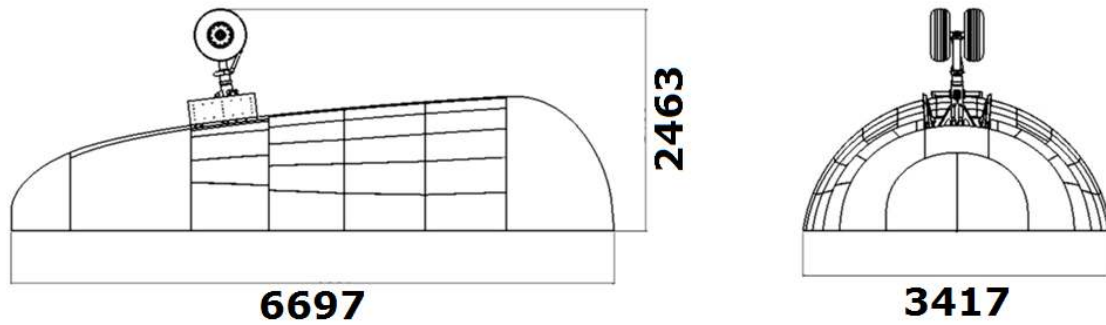


Figure 3: Main dimensions of wind-tunnel test model in mm [41].

1. For considering the acoustic results radiated in the *flyover* direction (i.e., for polar emission angles $\theta \approx 90^\circ$) the top array was employed (illustrated in Fig. 4a). The array consisted of 78 microphones in a multi-spiral arrangement of approximately 3 m diameter. This array was located in the $z = 4$ m plane, i.e., at a distance to the NLG axis of 1.825 m.
2. To study the lateral or *side* emission pattern of the NLG (i.e., for azimuthal angles $\phi \approx 90^\circ$) the side array was used (see Fig. 4b). The array was positioned in the $y = -4.22$ m plane, i.e. parallel to the model plane of symmetry and consisted of 66 microphones arranged in a half-wheel distribution with a diameter of approximately 3 m.

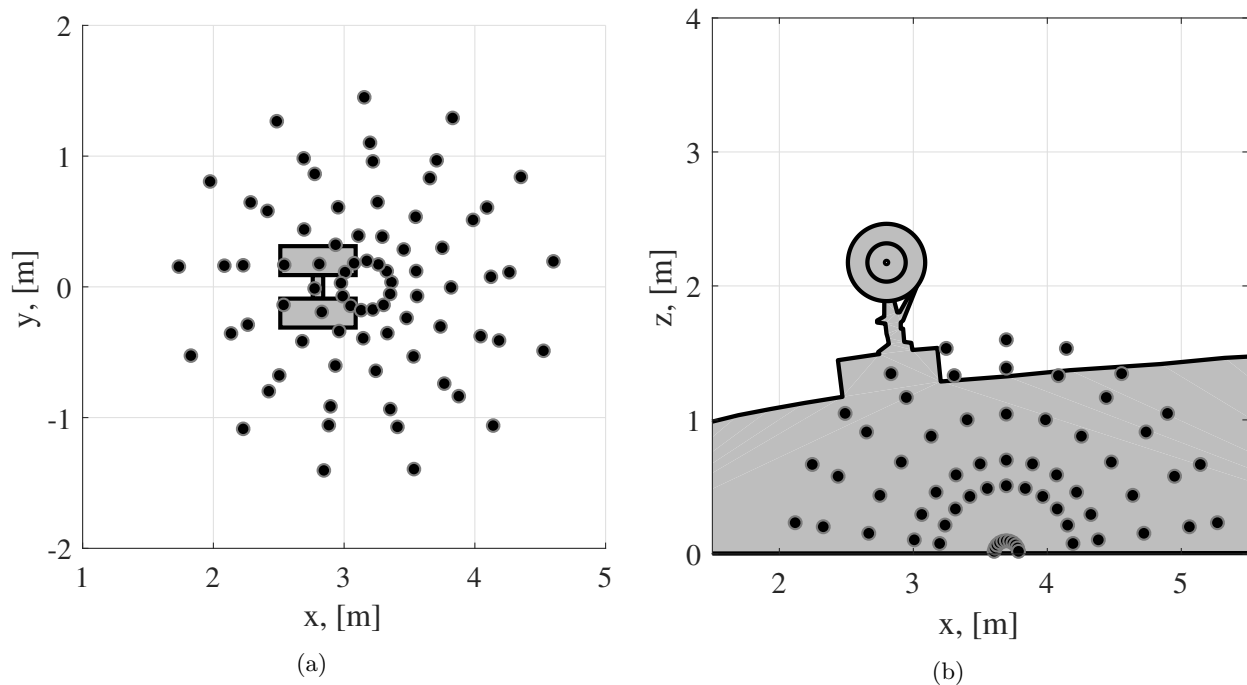


Figure 4: Microphone distribution for (a) the top array (b) the side array. A sketch of the ALLEGRA NLG model is plotted in gray for clarity reasons.

More details about the experimental setup can be found in the PhD thesis of Neri [41].

The data of both arrays were acquired simultaneously at a sampling frequency of 32,768 Hz for 10 s per measurement. The time-averaged cross-spectral matrix (CSM) [42] was obtained by using frequency spectra processed with a block length of 8192 samples, Hanning windowing and 50% data overlap, providing a frequency resolution Δf of 4 Hz.

The frequency range of interest considered for postprocessing extends from 200 Hz to 4000 Hz. The lower limit was defined by the background noise and the spatial resolution of the array in order to properly separate the sound coming from the NLG model from other noise sources. The higher frequency limit was imposed by the minimum distance between microphones to prevent aliasing, the amount of sidelobes, and the signal-to-noise ratio.

II.B. Flyover measurements

A total of 115 aircraft flyovers in their landing stage (as well as their respective aircraft types) were recorded in Amsterdam Airport Schiphol. Landing operations were preferred for this study since their flight trajectories are typically less variable than during takeoff, and especially because, during landing, turbofan engines normally operate at approach idle, making the identification of airframe noise sources (such as the NLG) more likely [24].

A phased microphone array consisting of 32 microphones distributed in a logarithmic spiral with a 1.7 m diameter was placed 1240 m away from the threshold of the Aalsmerbaan runway (36R), see Fig. 5. An optical camera was fixed to the center of the array facing straight up, which provided video footage synchronized with the microphone data. The weather conditions during the measurements were very similar and presented low wind speeds [43].

Out of these 115 flyovers, 36 correspond to regional airliners (approximately 30% of the total), confirming the importance of regional flights in European airports, such as Amsterdam Airport Schiphol. Data from three different regional aircraft types were selected for further analysis, which are referred to henceforth as Aircraft Types A, B and C, respectively, for confidentiality reasons. The NLG systems from these aircraft types have a similar geometry as the ALLEGRA model tested in the wind tunnel and computational simulations aforementioned, as will be discussed in Sec. II.D.

The array employed band filters to obtain frequencies between 45 Hz and 11,200 Hz. A sampling frequency of 40 kHz was used. For each measurement, 0.1024 s of data was considered for which the NLG is approximately overhead of the microphone array center (emission angle of $\theta \approx 90^\circ$, corrected for the source motion). The averaged CSM [42] is computed employing data blocks of 2048 samples and Hanning windowing with 50 % data overlap, providing a frequency resolution of approximately 20 Hz.

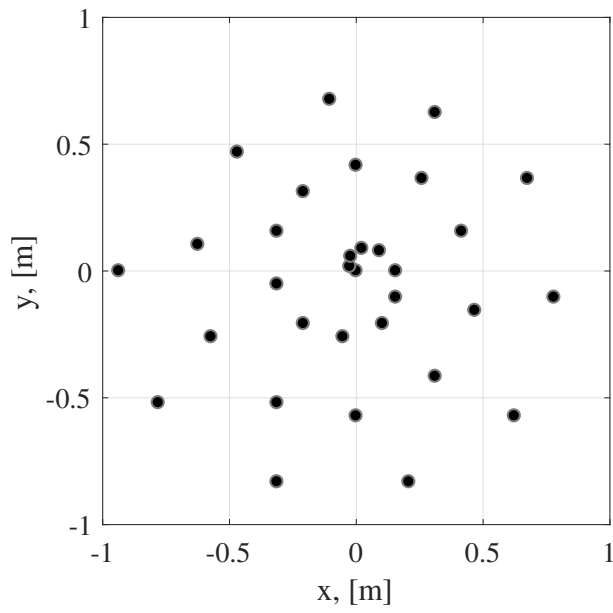
The frequency range selected for further analysis ranges from 1 kHz to 10 kHz. The lower bound was chosen for having enough spatial resolution to separate the sound coming from the NLG position from other noise sources on board, such as the turbofan engines. For the three aircraft types selected, the minimum distance between NLG and engines ranged from 12 m to 20 m, approximately. Aircraft Types A and C are equipped with rear-mounted engines, which allows for an easier separation of the NLG noise contribution. Aliasing and the amount of sidelobes determined the highest frequency of study, as for the wind-tunnel case.

The aircraft trajectories were calculated to account for the propagation effects from the source to the receiver. Data from three different sources [24] were used:

1. The Automatic Dependent Surveillance–Broadcast (ADS–B) (when available).
2. The radar from air traffic control (provided by Amsterdam Airport Schiphol).
3. The extrapolation of the images taken by the optical camera.

The three methods provided very similar results (with variations up to 6%), but the data from the optical camera were employed due to its availability and because it is easier to overlay the acoustic source plots to the pictures. The results from the other two methods were used as a validation. The average flight altitude and aircraft velocity above the array for the aircraft studied in this paper were 65.7 m and 69.3 m/s, respectively. Henceforth, true air speeds (considering the wind velocities) are presented in this paper.

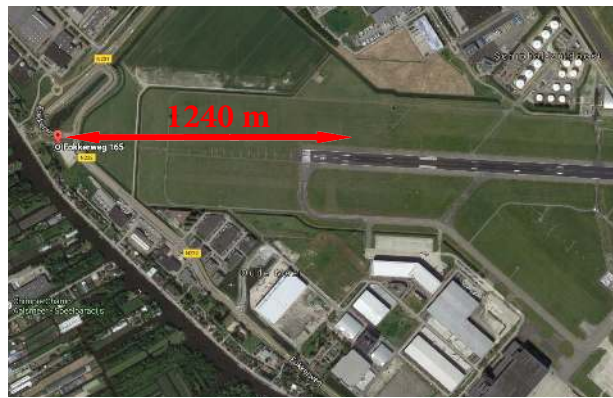
The Doppler effect was corrected according to Howell *et al.* [44] and the movement of the source was also later accounted for in the formulation of the beamforming algorithm [24, 39]. Finally, the geometrical spreading and the atmospheric absorption were also taken into account to obtain the L_p at the source position [1, 26]. A method for calculating the atmospheric absorption coefficient α was employed using the recorded ambient temperature, relative humidity and sound frequency [45].



(a)



(b)



(c)

Figure 5: (a) Microphone distribution for the array used in the flyover measurements. (b) Experimental setup at Amsterdam Airport Schiphol [24]. (c) Location of the microphone array with respect to the Aalsmeerbaan (36R) airport runway. The North is pointing to the right of the picture [20].

II.C. Computational simulations

Compressible flow simulations were performed using the commercial flow-solver STAR-CCM+ with an Improved Delayed Detached Eddy Simulation (IDDES) model [46]. A computational domain spanning 30 times the wheel diameter (d_{wheel}) in the streamwise direction, 18 d_{wheel} in the horizontal direction and 10 d_{wheel} in the vertical direction was used. Different mesh refinements were employed, with a higher grid density for meshes closer to the NLG smaller components [27]. The domain is discretized using an unstructured mesh with a total of 97 million hexahedral cells. The resolution of the mesh was sufficient to propagate the acoustic waves up to about 5000 Hz [27]. Volumetric quadrupole sources were neglected as it is commonly done for simulations featuring low Mach numbers. A detailed explanation about the computational setup and simulations is out of the scope of this paper. More information about the computational setup and the propagation analysis can be found in [27–29, 47].

The NLG geometry employed in the numerical simulations has been slightly simplified compared to the one used in the ALLEGRA wind-tunnel measurements: the bolts, nuts and air valves were removed from the wheels, since they included details that were deemed too small to be resolved correctly by the computational grid and were replaced with coarser versions [27]. Moreover, small gaps between parts were filled, in particular the gap at the center of the rim was filled to approximate the wheel bearings. Lastly, the position of the whole model considered was flipped upside down in the z direction compared to the wind-tunnel tests, see Fig. 6. Henceforth, only positive z coordinates are considered, even if the figures referring to the computational simulations display negative values of z . The fuselage belly was also included in the simulations, but is not illustrated in Fig. 6 for clarity reasons.

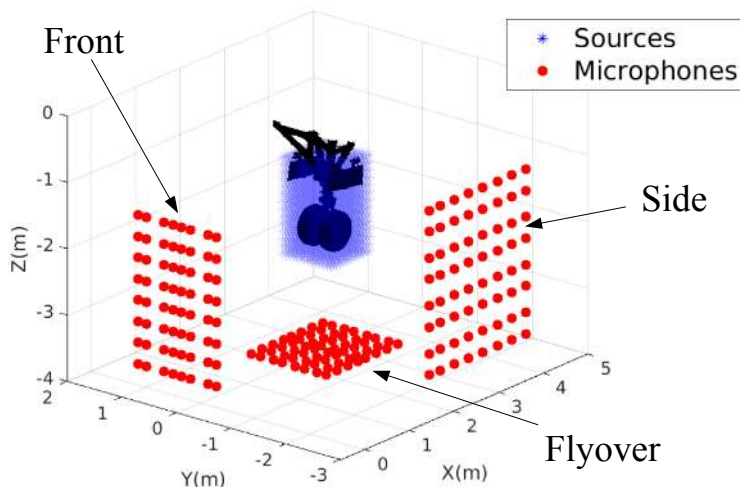


Figure 6: Position of the simulated ALLEGRA NLG model and the three virtual microphone arrays considered. Adapted from [27].

A uniform velocity field of $V_\infty = 50$ m/s was imposed at the inlet plane, a Dirichlet condition imposed the atmospheric pressure at the outlet plane and a no-slip condition was applied on the top plane of the computational domain, since it corresponds to the floor of the wind tunnel [27].

Five simulated acoustic arrays of 225 microphones (distributed in square grids of 15×15) were considered in the computational domain, see Fig. 6. The microphone coordinates were approximated to the nearest cell center available. These arrays were placed in the direct sound computation region, outside the unsteady region close to the NLG surface, where hydrodynamical waves were dominant. Hence, it was considered that at the arrays' positions, the acoustic field was the dominating fluctuating field [27]. The relative positions of each array with respect to the NLG model were:

1. *Flyover array*: Located at $z = 2.75$ m, i.e., 0.575 m away from the NLG axis, where the mesh spacing is 0.01 m.
2. *Side array 1*: Located at $y = -1$ m, i.e., 1 m away from the center of the NLG axis, where the mesh spacing is 0.02 m.

3. *Side array 2*: Located at $y = -0.4$ m, i.e., 0.4 m away from the center of the NLG axis, where the mesh spacing is 0.003 m.
4. *Front array 1*: Located at $x = 1.75$ m, i.e., 1.05 m away from the NLG axis, where the mesh spacing is 0.02 m.
5. *Front array 2*: Located at $x = 2.25$ m, i.e., 0.55 m away from the NLG axis, where the mesh spacing is 0.0025 m.

Different scan planes (parallel to the considered array) were used, and will be specified when presenting the results in Sec. V. All the scan grids consisted of 961 scan points disposed in a square fashion (31×31).

Apart from the signals recorded at the microphones arrays, the propagated far-field signals using the Ffowcs Williams–Hawkings (FW–H) analogy [48] at different observer positions located 1.5 m from the model are also considered.

The acoustic pressure data were extracted at all the microphone positions from 2500 samples at a sampling frequency of 20 kHz during 0.125 s (or 10 wheel convection cycles) [27]. The results were weighted using a Hanning windowing function and averaged using Welch’s method [42], providing a frequency resolution of approximately 39 Hz.

II.D. NLG geometries

In this subsection, the geometries of NLG of the ALLEGRA full-scale NLG model tested in the Pininfarina wind tunnel and the computational simulations, and those of the three regional aircraft types selected are presented. All the considered NLG geometries consist of a bogie structure with a single axis and two wheels. Table 1 contains the dimensions of the wheel diameter d_{wheel} , wheel width w_{wheel} and rim diameter d_{rim} for the four NLG geometries, as well as the technical denomination of the NLG (following the ISO metric tire code for flotation sizes) in each case. All the dimensions listed in Table 1 present similar values. Such small differences in the size of the NLG are not expected to cause considerable changes in the L_p values radiated (less than 1 dB) [15, 32].

Table 1: NLG geometry parameters [20].

Case	NLG type	d_{wheel} , [m]	w_{wheel} , [m]	d_{rim} , [m]
Aircraft Type A	24 × 7.7 10 12 PR	0.610	0.196	0.286
Aircraft Type B	24 × 7.7 16 PR	0.610	0.196	0.406
Aircraft Type C	19.5 × 6.75 – 8	0.495	0.172	0.203
ALLEGRA	22 × 8.0 – 10	0.577	0.221	0.286

The landing gear geometry designed within ALLEGRA, displayed schematically in Fig. 7, features a part of the fuselage, the gear bay, the doors and the gear assembly. The main elements of the NLG structure of the ALLEGRA model are depicted in Fig. 7 and listed with their names in Table 2.

III. Acoustic imaging methods

III.A. Method for the wind-tunnel experiments

Conventional frequency domain beamforming (CFDBF) was applied to the acoustic data of the top microphone array. The main diagonal of the CSM was removed in order to eliminate the influence of noise incoherent for all the microphones [39], such as wind noise. The convection of the sound waves due to the flow velocity was considered. A standard shear layer correction, as outlined by Amiet [49], was applied. The beamforming results were integrated over a region of integration (ROI) covering the NLG position, following the approach of the Source Power Integration technique (SPI) [39, 50]. The beamforming results were normalized by the integrated array response for a point source in the center of the ROI, also known as Point Spread Function (PSF). This way, more physical results are obtained, because the influence of the PSF in the results of the array is reduced [39, 51–55].

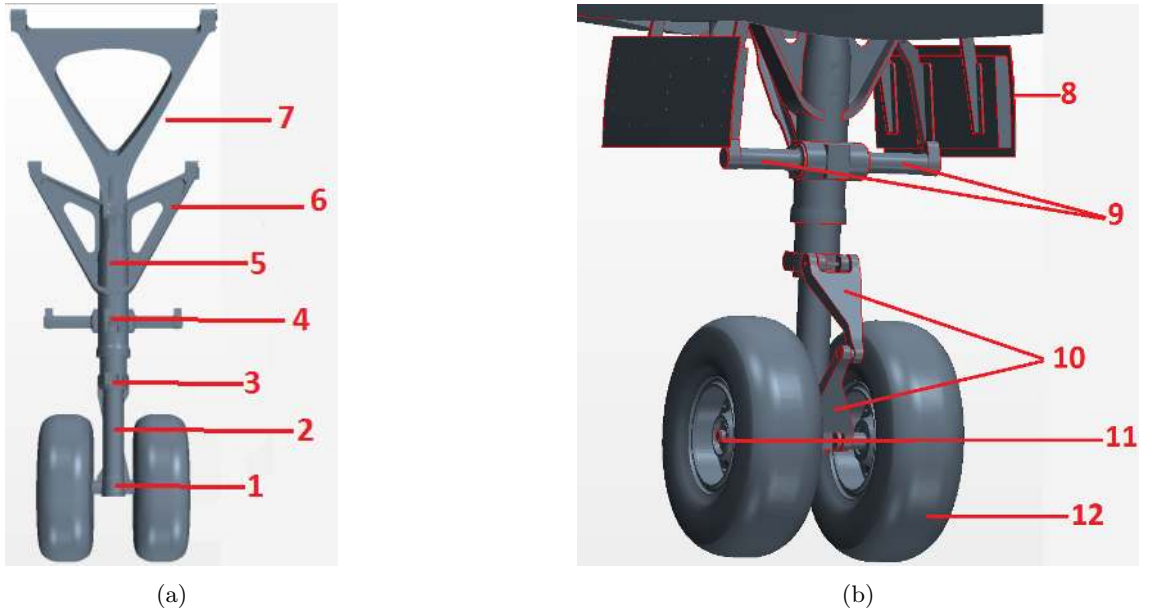


Figure 7: (a) View of the bare NLG assembly; (b) View of the back of the NLG assembly with bay doors and fuselage. Extracted from [27].

In addition, the high-resolution deconvolution method HR-CLEAN-SC [56–58] was also applied to the data from both arrays in order to obtain a better dynamic range (less and lower sidelobes) and to investigate whether one or more sound sources were present (even within Rayleigh resolution limit [56–58]). For the frequency range considered in the wind-tunnel measurements (200 Hz to 4 kHz), the differences between the obtained spectra by the SPI technique and HR-CLEAN-SC were small. Henceforth, the spectra obtained with HR-CLEAN-SC are presented in this paper.

III.B. Method for the flyover measurements

Functional beamforming [59, 60] was selected in this case, as it provides better dynamic range and array spatial resolution than CFDBF, and these features are very important for flyover measurements, due to the relatively large distance between source and observer [24, 26, 36]. Comparative studies with other acoustic imaging methods showed that functional beamforming [24, 38] provides better results when applied to flyover measurements.

The de-Dopplerized acoustic signals were employed and the movement of the source was taken into account in the beamforming formulation [24, 39, 61]. Removing the main diagonal of the CSM for this algorithm is prone to significant errors, since the method relies on the eigenvalue decomposition of the CSM [62]. For this experiment, however, it was not considered to be necessary to remove the main diagonal of the CSM, due to the low wind speeds and low background noise levels [24]. This method basically raises the CFDBF source plot to the power of an exponent parameter ν and the CSM to the inverse of this power $\frac{1}{\nu}$. The value of ν was chosen to be 32 after performing a sensitivity analysis [24, 36].

Additionally, an integration of the results over an area of interest located at the NLG position for each case was performed (see Fig. 10). The process is similar to the SPI technique aforementioned in Sec. III.A, where the beamforming results are now normalized by the PSF at the center of the integration area provided by functional beamforming.

III.C. Method for the computational simulations

The acoustic data extracted from the flow computations was propagated to simulated microphone arrays and processed using several beamforming approaches [27]. In this paper only results obtained with an adapted version of Linear Programming Deconvolution (LPD) [63], called dual-LPD [47], are presented. This method is essentially an alternative version of solving the inverse problem considered in deconvolution methods such

Table 2: Main elements of the landing gear. Extracted from [27].

Part Number	Part Name
1	Wheel axle
2	Main strut
3	Tow fitting
4	Lower arm joint
5	Drag stay Lower arm
6	Main fitting
7	Drag stay upper panel
8	Bay door
9	Steering pinions
10	Torque link
11	Wheel hub
12	Wheel

as DAMAS [64], but using linear programming. Deconvolution methods typically offer better dynamic range and spatial resolution than CFDBF, but require longer computational times.

Unfortunately, the absolute spectra obtained by the simulated microphone–array measurements were not available for confidentiality reasons. Hence, only source maps depicting the location of the identified sound sources and two far–field sound spectra are presented in this manuscript for comparison purposes.

IV. Noise prediction models

This section briefly describes two common airframe noise prediction models currently used to predict LG noise. The focus is kept on semi–empirical and semi–analytical noise models typically used for fast estimation of aircraft noise during aircraft design and parametric sensitivity studies, to quantify changes in noise impact due to changes to the aircraft geometry. These models are typically developed based on wind–tunnel or flight measurements of several aircraft and are averaged or normalized to reflect the typical noise spectra and directivities of generic aircraft geometries. As such, their accuracy is limited within a small range of the measurement database on which they are based on. Nonetheless, the models described here have been used extensively by organizations worldwide to assess the community noise impact of various aircraft designs, as well as flight procedures and routes. The computational efficiency of the models to compute the noise impact, in the range of seconds for selected observer points and minutes for ground grids needed to make noise contours, has led to their continuing, widespread use in the noise modeling and prediction communities. Two of the most frequently used models for predicting landing gear noise, that of Fink [18] and Guo [31, 32] are explained here. It should be noted that these models use imperial units, i.e., inches for lengths and knots for the velocity.

IV.A. Fink’s model

Fink’s method [18] was developed for the US Federal Aviation Agency (FAA) and has been implemented in NASA’s Aircraft Noise Prediction Program (ANOPP) framework [65, 66]. Fink assumes that there are two primary noise sources on the landing gear: the strut of the gear and the wheels, based on experimental data from flyover measurements of several aircraft [3]. Therefore, the input parameters required for this method are just the mean flow velocity V_∞ , the number of wheels N_{wheel} , the wheel diameter d_{wheel} and the strut length l_{strut} . The various interaction effects of the wheels and strut with each other as well as with other airframe components are, thus, neglected. The generic form of the mean–squared, far–field acoustic pressure for all airframe noise components according to Fink’s method is given by

$$\langle p^2 \rangle = \frac{\rho c P \hat{D} \hat{F}}{4\pi r^2 [1 - M \cos(\theta)]^4}, \quad (1)$$

where ρ is the air density, c is the speed of sound, P is the sound power of each component (wheel and strut), \hat{D} is the directivity function, \hat{F} is the spectrum function and r is the distance between source and observer. The term between brackets $[1 - M \cos(\theta)]^4$ is the convective amplification factor due to the motion of the source [24], where M is the Mach number: $M = V/c$, where V is the source velocity.

The sound power for the wheel noise is defined as

$$P_{\text{wheel}} = K_1 M^6 N_{\text{wheel}} d_{\text{wheel}}^2, \quad (2)$$

where $K_1 = 4.349 \times 10^{-4}$ for two-wheel LG systems (typically for NLG) and $K_1 = 3.414 \times 10^{-4}$ for four-wheel LG systems (typically for MLG). The term M^6 refers to the expected 6th power law with the flow velocity [67].

The sound power for the strut noise is defined as

$$P_{\text{strut}} = K_2 M^6 d_{\text{wheel}} l_{\text{strut}}, \quad (3)$$

where $K_2 = 2.753 \times 10^{-4}$. The contributions of both components are typically of comparable order of magnitude.

The directivity functions for each component are calculated using

$$\hat{D}_{\text{wheel}} = \frac{3}{2} \sin^2 \theta, \quad (4)$$

$$\hat{D}_{\text{strut}} = 3 \sin^2 \theta \sin^2 \phi, \quad (5)$$

where θ is the polar emission angle and ϕ is the azimuthal sideline noise emission angle [18]. The case of $\phi = 0^\circ$ corresponds to the direction directly under the landing gear and $\phi = 90^\circ$ corresponds to the wheel axis pointing to the right. With this angle criteria, and according to Eq. (5), the strut does not contribute to the overall noise emissions directly under the landing gear ($\phi = 0^\circ$).

The spectrum function \hat{F} depends on the component and N_{wheel} , as well as on the Strouhal number based on the wheel diameter [18], $St = \frac{f d_{\text{wheel}}}{c}$. Equation (6) represents the spectrum function depending on several empirical parameters (\hat{A} , \hat{B} , \hat{q} , $\hat{\mu}$ and $\hat{\sigma}$), which can be found for each component in Table 3.

$$\hat{F} = \frac{\hat{A} St^{\hat{\sigma}}}{(\hat{B} + St^{\hat{\mu}})^{\hat{q}}}, \quad (6)$$

Table 3: Required empirical parameters for Fink's noise prediction method.

Component	\hat{A}	\hat{B}	\hat{q}	$\hat{\mu}$	$\hat{\sigma}$
Wheel ($N_{\text{wheel}} = 2$)	13.58	12.5	2.25	2	2
Wheel ($N_{\text{wheel}} = 4$)	0.0577	1	1.5	2	2
Strut ($N_{\text{wheel}} = 2$)	5.325	30	1	8	2
Strut ($N_{\text{wheel}} = 4$)	1.28	1.06	3	2	3

Hence, the total LG noise emissions can be calculated by summing the contributions of the wheel assembly and the strut introducing Eqs. (2) to (6) into Eq. (1).

IV.B. Guo’s model

Also known as the “Boeing” method, Guo’s method [31, 32] is based on fundamental aerodynamic noise theory and scaling laws adjusted to fit full-scale LG aeroacoustic tests [34]. In order to include more physics than Fink’s method, this technique considers three different types of LG components depending on their size, each of them contributing in a different frequency range:

1. **Large-scale structures** such as the wheels, contributing to the low-frequency noise.
2. **Mid-scale structures** such as the main struts, contributing to the mid-frequency noise.
3. **Small-scale structures** such as the hydraulic lines and LG dressings, contributing to the high-frequency noise.

These three components are considered separately with a different spectral shape and directivity. For this purpose, more detailed geometrical inputs of the LG are required for this method, compared to Fink’s method. Hence, Guo’s method is expected to provide higher-fidelity noise predictions.

The far-field mean-square acoustic pressure can be estimated as

$$\langle p^2 \rangle = \frac{\rho^2 c^4 M^6 \hat{D}_{\text{overall}}}{r^2 [1 - M \cos(\theta)]^4} (P_{\text{low}} + P_{\text{mid}} + P_{\text{high}}), \quad (7)$$

where P_{low} , P_{mid} and P_{high} represent the sound powers of the low, mid and high frequency components, respectively. \hat{D}_{overall} is the overall directivity function, in addition to the directivity function included in each P term, which accounts for the installation effects of the LG. The presence of the wing and fuselage of the aircraft causes reflection and diffraction [32], which will enhance the noise radiation, especially in the overhead direction ($\theta = 90^\circ$). This parameter can be estimated using the following empirical expression

$$\hat{D}_{\text{overall}} = 1.2(1 - 0.9 \cos^2 \theta)^2. \quad (8)$$

Each of the P terms in Eq. (7) are defined as

$$P = \beta S \hat{D} \hat{F}, \quad (9)$$

where β is the flow energy conversion efficiency parameter (see Table 4) and S is the aggregate surface integration effects [32], which depends on the geometry of the LG components:

$$S_{\text{low}} = \pi N_{\text{wheel}} w_{\text{wheel}} d_{\text{wheel}}, \quad (10)$$

$$S_{\text{mid}} = \sum_{k=1}^{N_{\text{strut}}} \hat{s}_{\text{strut},k} l_{\text{strut},k}, \quad (11)$$

$$S_{\text{high}} = \hat{\eta} l_{\text{high}}^2, \quad (12)$$

where w_{wheel} is the wheel width, N_{strut} is the number of main struts in the LG assembly, $\hat{s}_{\text{strut},k}$ and $l_{\text{strut},k}$ are the perimeter of the cross section and the length of the k^{th} strut, respectively. The dimensionless parameter $\hat{\eta}$ is the complexity factor accounting for the geometric complexity of the small-scale components of the LG. This parameter has a complicated expression depending on the takeoff weight of the aircraft, but for NLG, $\hat{\eta}$ can be approximated by a constant value of 0.1 [32], since a typical NLG is much simpler than a MLG and their complexity does not vary significantly within different aircraft types. The characteristic length of the small-scale components l_{high} can be approximated as

$$l_{\text{high}} = 0.15 \frac{S_{\text{mid}}}{\pi \sum_{k=1}^{N_{\text{strut}}} l_{\text{strut},k}}. \quad (13)$$

The Strouhal number is defined for each frequency range

$$St_{\text{low}} = \frac{f d_{\text{wheel}}}{V}, \quad (14)$$

$$St_{\text{mid}} = \frac{fS_{\text{mid}}}{\pi V \sum_{k=1}^{N_{\text{strut}}} l_{\text{strut},k}}, \quad (15)$$

$$St_{\text{high}} = \frac{fl_{\text{high}}}{V}, \quad (16)$$

The spectrum function \hat{F} can be calculated in a similar way as for Fink’s method (see Eq. (6)) using the parameters gathered in Table 4.

Table 4: Required empirical parameters for Guo’s noise prediction method.

Frequency	\hat{A}	\hat{b}	\hat{B}	\hat{h}	\hat{q}	$\hat{\beta}$	$\hat{\mu}$	$\hat{\sigma}$
Low	3.53	3	0.62	0.2	2.6	4.5×10^{-8}	2.5	4
Mid	0.42	2	0.18	0.6	4.2	1.5×10^{-8}	1.5	3
High	0.08	0.1	0.1	1	4.2	3.2×10^{-5}	1.1	2

The frequency–dependent directivity function \hat{D} can be defined as

$$\hat{D} = (1 + \hat{h} \cos^2 \theta)^2 (1 + \hat{b} \sin^2 \phi)^2, \quad (17)$$

where \hat{h} and \hat{b} are empirical constants [34] whose values are listed in Table 4. This directivity pattern peaks at the upstream and downstream directions and shows a minimum near the overhead direction ($\theta \approx 90^\circ$). Moreover, as the frequency increases, the radiation pattern becomes more directional in the polar direction [32]. In the azimuthal direction, the maximum emission direction corresponds to $\phi = 90^\circ$.

The effect of the lower flow velocity impinging at the MLG compared to the NLG is also accounted for [17]. With all these equations, all the P terms in Eq. (7) can be calculated and the far–field noise emissions can be obtained.

The predictions of this method have been shown to compare well with experimental data from wind–tunnel and flight measurements [32, 34], both in parametric trends and absolute noise levels.

V. Experimental results

V.A. Acoustic imaging results

The acoustic imaging results obtained can be divided in three categories depending on the emission direction considered, see Fig. 6: flyover (in the z direction, as considered for the flyover measurements), side (in the y direction) and front (in the x direction).

V.A.1. Flyover direction

Figure 8 depicts three CFDBF source plots of the ALLEGRA NLG corresponding to the wind–tunnel measurements with a flow speed of 50 m/s and to the one–third–octave bands with center frequencies of 630 Hz, 1250 Hz and 2000 Hz, respectively. The scan plane used was parallel to the top microphone array, at a distance of 1.825 m from it (i.e., at $z = 2.175$, containing the wheel axis). Figure 9 contains the results corresponding to the same conditions as in Fig. 8 after applying HR–CLEAN–SC, which offers clearer source plots. In both figures, it seems that the dominant noise source for all frequency cases is located slightly upwind from the center of the wheel axis, between both wheels. The dashed rectangle denotes the ROI. At the highest frequency (2 kHz), the sound source seems to be more distributed over the whole NLG structure, covering some regions of the downwind side of the wheels. This could be due to the vortex shedding generated by the wheels [4]. However, sound sources could be located anywhere along the vertical line passing through the middle point of the axis, since the resolution of the microphone array in the normal direction (z direction) is not so accurate to localize the source within the axis. Thus, it is also possible that the main sound source is located on the strut of the NLG or thereabouts.

Figure 10 illustrates an example functional beamforming source plot for a flyover measurement of each of the three aircraft types aforementioned. It is observed that the NLG is always the dominant noise source for the frequency range selected (one–third octave band centered at 2 kHz). This frequency band was selected

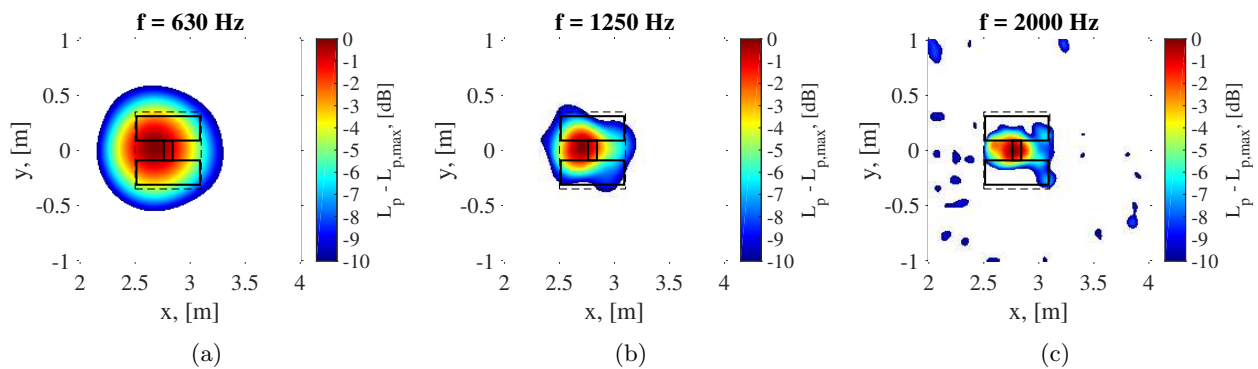


Figure 8: One-third-octave band CFDBF source plots for the ALLEGRA NLG model (*flyover* view) at a flow velocity of $V = 50$ m/s and a center frequency of (a) 630 Hz; (b) 1250 Hz; (c) 2000 Hz. The schematic position of the ALLEGRA NLG model is depicted as solid black lines and the dashed rectangle denotes the ROI.

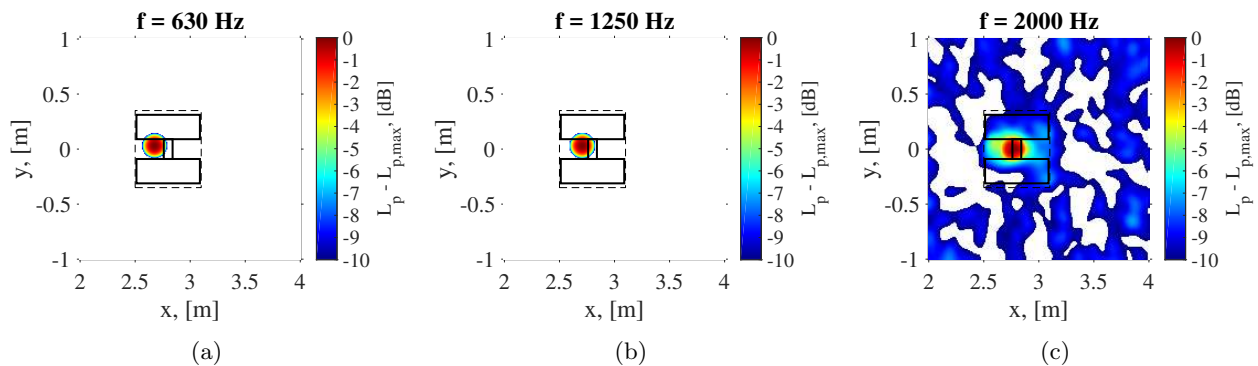


Figure 9: One-third-octave band HR-CLEAN-SC source plots for the ALLEGRA NLG model (*flyover* view) in the wind tunnel at a flow velocity of $V = 50$ m/s and a center frequency of (a) 630 Hz; (b) 1250 Hz; (c) 2000 Hz. The schematic position of the ALLEGRA NLG model is depicted as solid black lines and the dashed rectangle denotes the ROI.

due to the presence of strong tonal noise, as it will be shown in Sec. V.B. The dashed rectangles again denote the ROIs. For Aircraft Type B (Fig. 10 (b)) an additional sound source is localized at what appears to be the flap side edge of the left wing. For this example the outline of the aircraft has been manually added for clarity, because the sunshine blurred the picture.

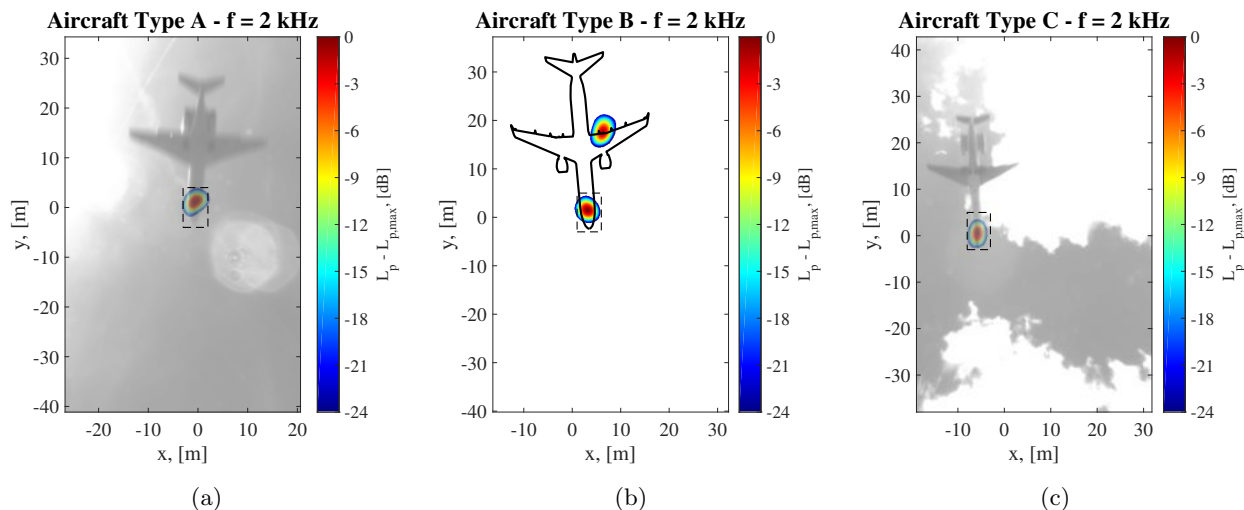


Figure 10: One-third octave band (2 kHz) functional beamforming source plots for each aircraft type using $\nu = 32$. (a) Type A; (b) Type B (aircraft outline has been added for clarity); (c) Type C. The dashed rectangles denote the respective ROIs.

Two source plots obtained from the computational simulations in the flyover direction with the *Flyover* array are depicted in Fig. 11 for the one-twelfth-octave band with center frequencies of 1200 Hz and 2300 Hz, respectively. The scan plane was located at $z = 2.5$ m. Although the source plots obtained by dual-LPD present a more *discontinuous* distribution, the locations of the dominant sound sources agree with those found in the wind-tunnel experiments, see Figs. 8 and 9, i.e., between both wheels. Once again, for the highest frequency (2300 Hz), the sound sources seem to be more distributed, including some areas of the downwind side of the wheels.

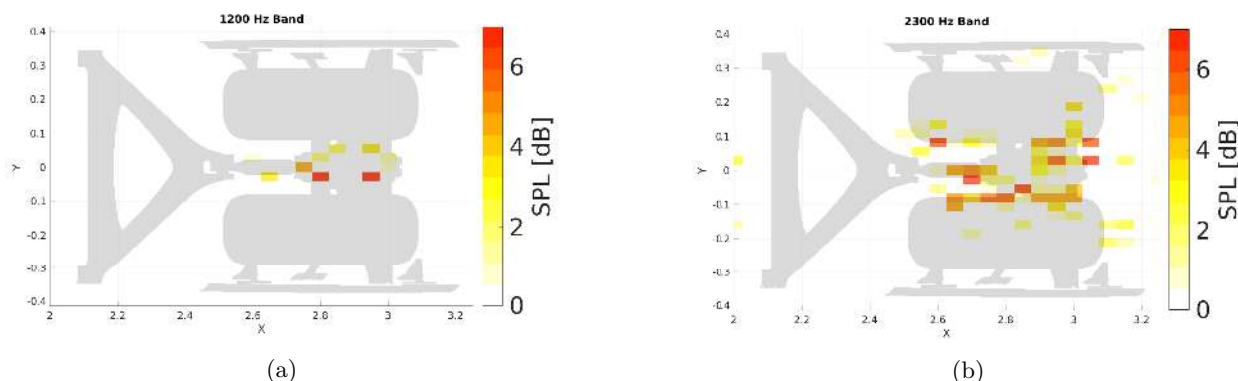


Figure 11: One-twelfth-octave band dual-LP source plots for the ALLEGRA NLG model (*flyover* view) in the computational simulations at a flow velocity of $V = 50$ m/s and a center frequency of (a) 1200 Hz and (b) 2300 Hz. Extracted from [27].

V.A.2. Side direction

The source plots corresponding to the side array in the ALLEGRA wind-tunnel experiments are presented in Figs. 12 and 13, for CFDBF and HR-CLEAN-SC, respectively. The same conditions as in Figs. 8 and 9 are considered (a flow speed of 50 m/s and one-third-octave bands with center frequencies of 630 Hz, 1250

Hz and 2000 Hz). The scan plane used was parallel to the side microphone array, at a distance of 4.2 m from it (i.e., at $y = 0$ containing the center of the wheel axis).

Once again, HR-CLEAN-SC provides clearer source plots, which are used to determine the location of the dominant sound sources. For the 630 Hz frequency band, it seems that the dominant sound source is located close to the rim of the wheel, next to the wheel axle. For the frequency bands centered at 1250 Hz and 2000 Hz, the main noise source seems to be located near the tow fitting (see Fig. 7). The presence of the wheels might shield potential sources located exactly at the axle in the *side* direction. Once again, the positions of the sound sources seem to be shifted slightly upwind, which could be caused by an error in the determination of the flow speed. For this emission direction, two different ROIs were defined (denoted as dashed rectangles in Figs. 12 and 13), one covering the wheel and the other covering the main strut and the bay door. This way, the contributions of each region can be separated.

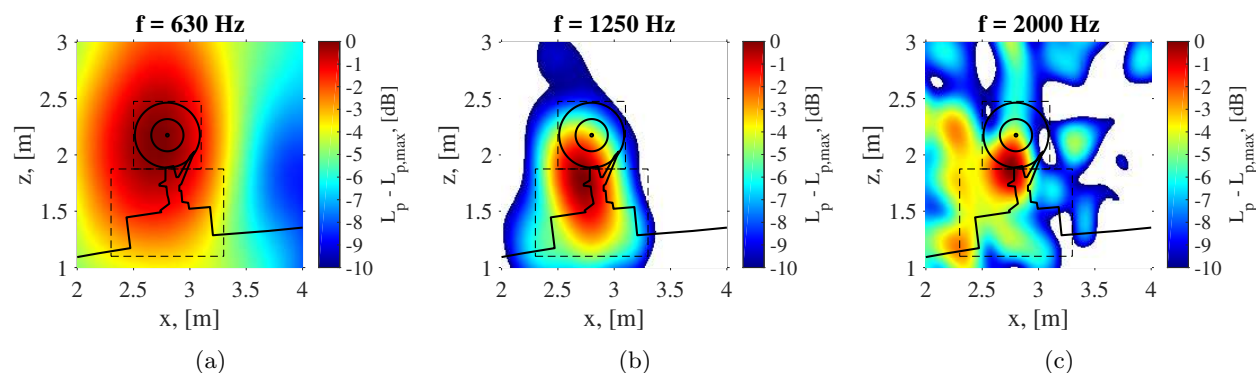


Figure 12: One-third-octave band CFDBF source plots for the ALLEGRA NLG model (*side* view) at a flow velocity of $V = 50$ m/s and a center frequency of (a) 630 Hz; (b) 1250 Hz; (c) 2000 Hz. The position of the ALLEGRA NLG model is depicted as solid black lines and the dashed rectangles denote the respective ROIs.

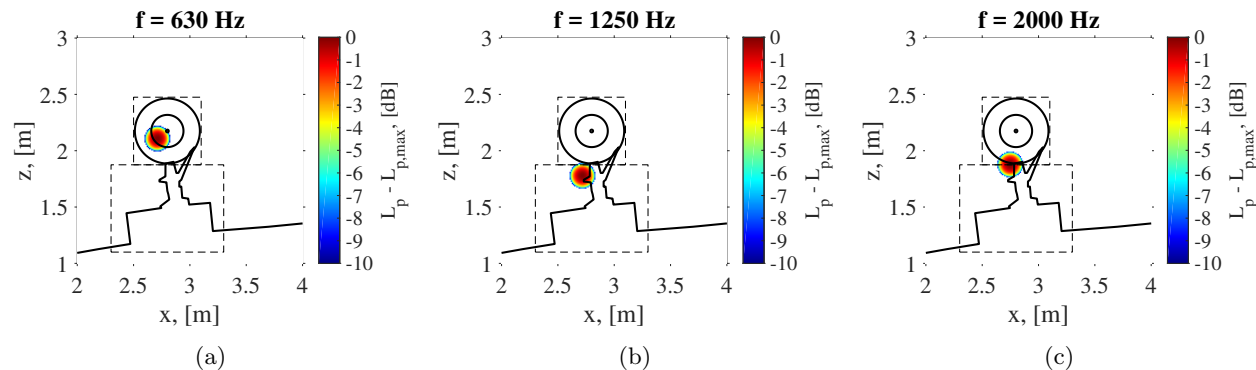


Figure 13: One-third-octave band HR-CLEAN-SC source plots for the ALLEGRA NLG model (*side* view) at a flow velocity of $V = 50$ m/s and a center frequency of (a) 630 Hz; (b) 1250 Hz; (c) 2000 Hz. The position of the ALLEGRA NLG model is depicted as solid black lines and the dashed rectangles denote the respective ROIs.

Figure 14 contains two source plots obtained from the computational simulations in the side direction for the one-twelfth-octave band with center frequencies of 1200 Hz and 2400 Hz, obtained by the *Side array 1* and the *Side array 2*, respectively. The scan plane was located at $y = -0.3$ m. For the band centered at 1200 Hz, the sound sources seem to be clustered along the tow fitting, the lower arm joint and the torque link, which agrees with the wind-tunnel results. For the case of 2400 Hz, on the other hand, the dominant sound source is located at the upwind part of the bay door.

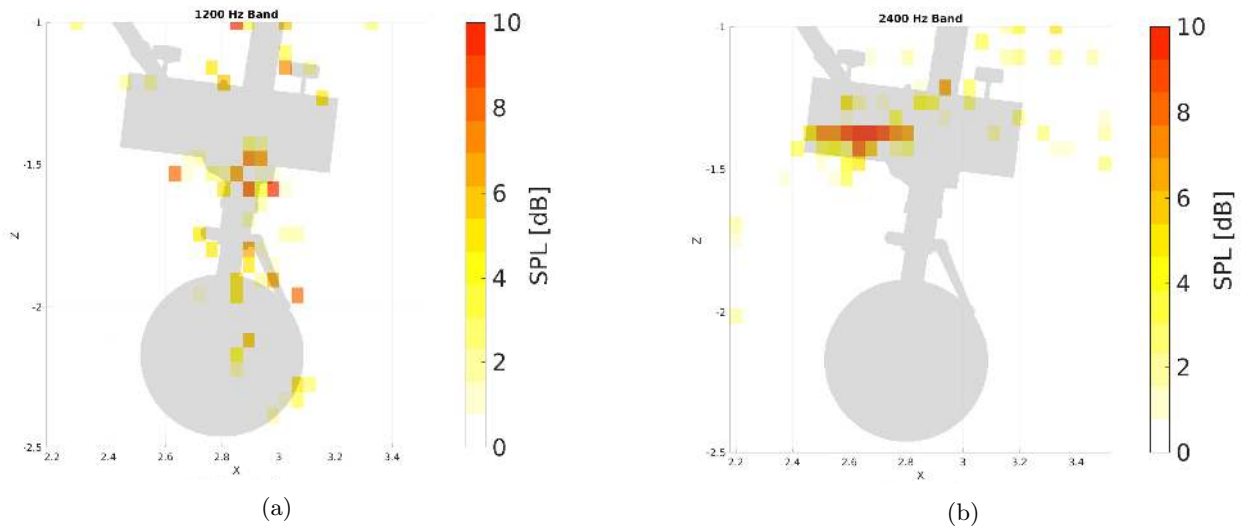


Figure 14: One-twelfth-octave band dual-LP source plots for the ALLEGRA NLG model (*side view*) in the computational simulations at a velocity of $V = 50$ m/s and a center frequency of (a) 1200 Hz obtained with *Side array 1*, and (b) 2400 Hz obtained with *Side array 2*. Extracted from [27].

V.A.3. Front direction

As aforementioned, the computational simulations allow for the non-intrusive placement of virtual microphone arrays to study emission directions that would be impractical to measure in wind tunnels. Figure 15 shows the simulated source plots in the front direction for one-twelfth-octave band with center frequencies of 1000 Hz and 2400 Hz obtained by the *Front array 1* and *Front array 2*, respectively. The scan plane was located at $x = 2.826$ m. For the first case, the strongest noise source is located in the center of the wheel axle, whereas for the second band, the sources are more spread in the center of the wheel axle, the lower arm joint and the bay doors. The bay door was also a dominant noise source for the side direction at that frequency, see Fig. 14b.

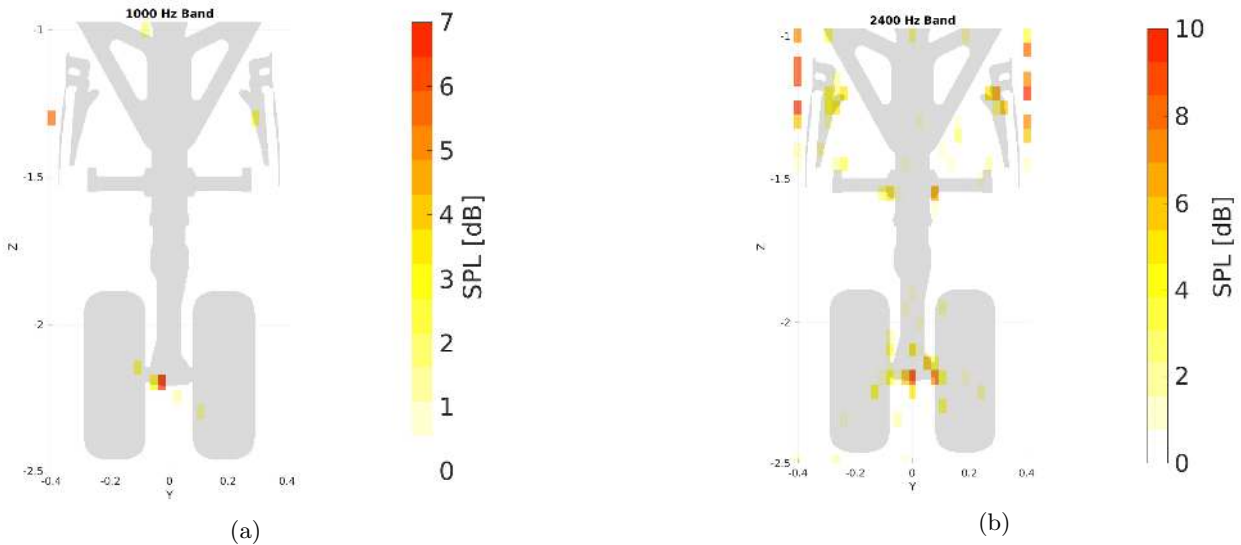


Figure 15: One-twelfth-octave band dual-LP source plots for the ALLEGRA NLG model (*front view*) in the computational simulations at a flow velocity of $V = 50$ m/s and a center frequency of (a) 1000 Hz obtained with *Front array 1*, and (b) 2400 Hz obtained with *Front array 2*. Extracted from [27].

V.B. Frequency Spectra Comparison

V.B.1. Correlation with flow velocity

The noise emissions from a LG system are expected to follow a 6th power law with the flow velocity [4, 10, 15, 18], considering a compact dipole noise generation mechanism due to unsteady forces [31] and assuming that the sound wavelength is comparably larger than the dimensions of the sound source.

A previous experimental study [20] showed that the ALLEGRA model and the Aircraft Type A follow power laws with respect to the flow velocity with exponents of 5.90 and 5.93, respectively. Therefore, the 6th power law is considered for both data sets, henceforth:

$$L_{p,V} - L_{p,V_{\text{ref}}} \approx 60 \log \left(\frac{V}{V_{\text{ref}}} \right) \quad (18)$$

where V_{ref} denotes an arbitrary reference velocity.

An illustrative example that confirms the considered power law is presented in Fig. 16a, where the integrated HR–CLEAN–SC narrow–band frequency spectra for the ALLEGRA model in the flyover direction for the four flow velocities are presented. When the spectra are corrected following the 6th power law and taking 40 m/s as the reference velocity V_{ref} , all the spectra collapse in one single line with only small differences at around 2500 Hz, see Fig. 16b. All the spectra are mostly broadband with just few tonal components below 500 Hz, but they do not protrude a lot over the broadband levels around them.

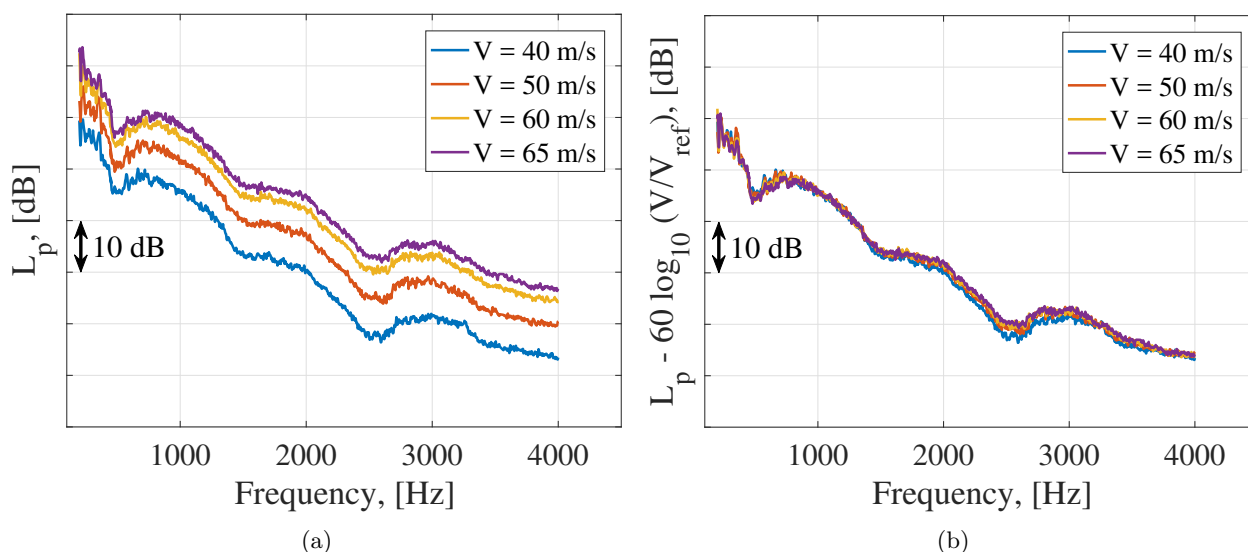


Figure 16: (a) Integrated frequency spectra for each velocity of the ALLEGRA NLG model in the wind–tunnel tests in the flyover direction. (b) Idem for the spectra converted to $V_{\text{ref}} = 40$ m/s using the obtained velocity power law.

For high frequencies, the LG cannot be considered as compact with respect to the sound wavelength anymore and more sophisticated power laws can be derived [68], featuring an exponent of 7 instead of 6, because the noise generation is considered to be due to the turbulent flow surrounding the small components of the LG. Since the effective frequency range for comparison in this paper (1 kHz to 4 kHz) is relatively low–frequency, this aspect was not considered.

V.B.2. Flyover direction

This section compares the noise emissions of the NLG in the flyover direction. Figure 17a presents the A–weighted sound pressure levels ($L_{p,A}$) of the integrated narrow–band frequency spectra (corrected for the velocity influence taking $V_{\text{ref}} = 65$ m/s) of an example flyover of each aircraft type, as well as the spectrum for the ALLEGRA model in the wind tunnel at $V = 65$ m/s. Similar trends are observed between the wind–tunnel and the flyover results. Unfortunately, the portion of the spectrum where both wind–tunnel and flyover results overlap is limited (1 kHz to 4 kHz). Other flyover measurements of these aircraft types were

similar to the ones presented here, but are not included for the sake of simplicity. Since the aircraft velocities are of the same order for the four cases shown in Fig. 17a, as well as the NLG geometries, differences in the Reynolds number are expected to be negligible. The differences between the wind–tunnel results and the flyover measurements could be due to several reasons, such as installation effects or different propagation conditions [22].

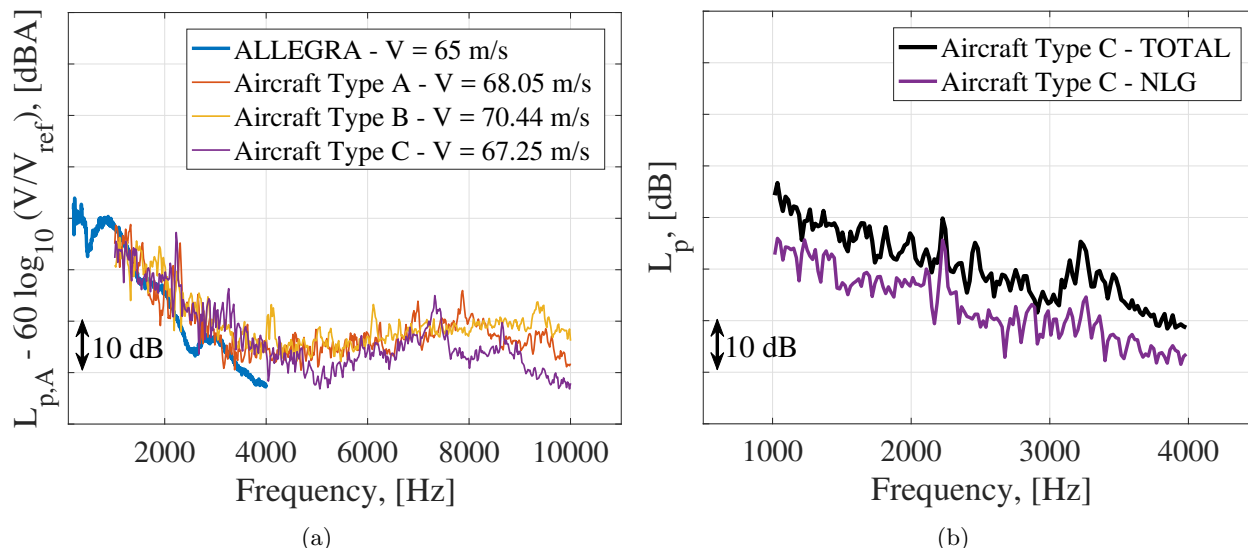


Figure 17: (a) Integrated A–weighted narrow–band frequency spectra of the NLG for an example flyover of each aircraft type. The spectrum of the ALLEGRA model with $V_{\text{ref}} = 65$ m/s is also plotted for comparison. (b) Zoomed–in spectra comparison for an Aircraft Type C flyover between the NLG and the total aircraft ($V = 67.25$ m/s)

It can be noticed that strong tonal noise is present for the three aircraft types at approximately 2200 Hz. This is especially the case for Aircraft Type C, for which a tone, protruding more than 12 dB higher over the broadband noise around it, is found. This phenomenon was already observed for other full–scale aircraft types by Michel and Qiao [10], by Dedoussi *et al.* [16] and by Merino–Martínez *et al.* [19, 24] and for wind–tunnel experiments featuring scale [3] or full–scale landing gears [15]. In some of these publications, it was suggested that the cause for these tonal peaks was the presence of open pin–cavities in the LG system. For the case of [15], it was determined that one of the main sources of tonal noise was the cavity of the pin that links the brakes and the brake–rods. The fact that no dependency was found between the tone frequency and the aircraft velocity (unlike with Aeolian tones) confirms the likelihood that these tones originate from a cavity [10, 16]. Since the geometries of the NLG for the three aircraft are similar, it is possible that they have cavities of similar dimensions as well, generating tones with comparable wavelengths. In addition, previous measurements with flyover measurements featuring larger NLG geometries [19] presented tonal noise at lower frequencies (approximately 1700 Hz) and hence, larger wavelengths. The ratio between the wavelengths of the tonal noise of the experiment in [19] and the one of the present study agrees with the ratio between the axle lengths, providing more evidence that the tonal noise is likely to be due to a cavity. On the other hand, no significant tones were present in the ALLEGRA model in this frequency range. This may be because cavities were intentionally designed out of the model.

For the measured flyovers, the aforementioned tones were also present in the overall spectra of the whole aircraft, indicating the importance of NLG noise at around 2200 Hz. This is illustrated in Fig. 17b for the same flyover measurement of an Aircraft Type C as in Fig. 17a, where the NLG spectrum is compared to the total aircraft sound spectrum obtained using a single microphone and correcting for the propagation effects [43]. The tone at 2200 Hz is also present in the total aircraft spectrum. Removing the tone at that frequency would cause overall L_p reductions up to 1 dB (up to 2 dB if A–weighting is considered) for the frequency range considered. In addition, tonality is of high importance when assessing aircraft noise around airports, since it has been shown that tonal noise causes significantly more annoyance than broadband noise with the same $L_{p,A}$ [69–71].

The far–field acoustic spectra obtained by the *Flyover array* in the computational simulations are pre-

sented in Fig. 18, where the Direct Numerical Beamforming (DNB) results using dual-LPD are shown, as well as the propagated signal using the FW-H analogy. The three different lines for DNB refer to how the deconvolution approach is performed: from below (DNB_b), from above (DNB_a) or in the optimal way (DNB_o). For further explanations, the reader can refer to [27].

It can be observed that the three DNB approaches present a strong tonal peak (protruding about 20 dB over the surrounding broadband noise) approximately at 2100 Hz, which agrees with the tonal peaks found in the flyover measurements displayed in Fig. 17. The FW-H results, however, only present a tonal peak at about 1050 Hz, which is coincidentally half of the tonal frequency for DNB. The reason for this difference remains unknown and is subject for future research.

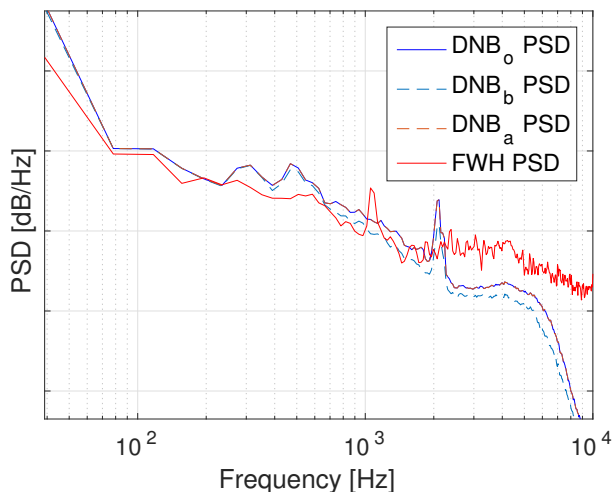


Figure 18: Far-field acoustic spectra obtained by the *Flyover array* in the computational simulations with DNB and the FW-H analogy. The grid step in the ordinate axis is 20 dB. The observer for the FW-H analogy is located at (2.826 m, 0 m, 3 m). Extracted from [27].

Figure 19a presents the comparison between the one-third-octave band spectra of the NLG emissions of three aircraft types, the ALLEGRA NLG from the wind-tunnel experiments (as presented in Fig. 17a) and the estimations of the two noise prediction models considered (Fink and Guo) using the geometry inputs of the ALLEGRA NLG model and a flow velocity $V = 65$ m/s. A first observation in the frequency range of common comparison (1 kHz to 4 kHz) indicates that Guo’s model has a better fit with the experimental data (especially with the flyover measurements) and that Fink’s model tends to overpredict the noise emissions in this case by several dB. Neither of the two noise prediction models seem to include the tonal peak at around 2 kHz as expected, but they also do not consider the noise increase at higher frequencies (after 5 kHz). The wind-tunnel results present a *hump* between 500 Hz and 1600 Hz that is not captured by the noise prediction models either. Moreover, the relatively high noise levels at low frequencies observed for the ALLEGRA NLG could be explained by the higher background noise levels at the wind-tunnel facility at that frequency range.

The integrated noise values in the frequency range between 1 kHz to 4 kHz predicted by Guo are considerably closer to those measured in the flyover experiments (within approximately a 1.5 dB difference), while the predictions by Fink are approximately 4 dB higher than the flyover experiments.

Figure 19b depicts the same results as Fig. 19a but using the normalized frequency axis with the Strouhal number based on the wheel diameter ($St = f \cdot d_{\text{wheel}}/V$). In this case, the broadband frequency components after $St > 20$ of the three aircraft types seem to collapse in a better way, but the tonal peaks are now slightly more spread in different Strouhal numbers.

V.B.3. Side direction

The integrated frequency spectra in the side direction for each of the ROIs defined in Figs. 12 and 13, namely the wheel and the strut and bay door of the ALLEGRA NLG, respectively, are presented in Fig. 20a, as well as the total NLG emissions. The spectrum of the ALLEGRA NLG in the flyover direction from

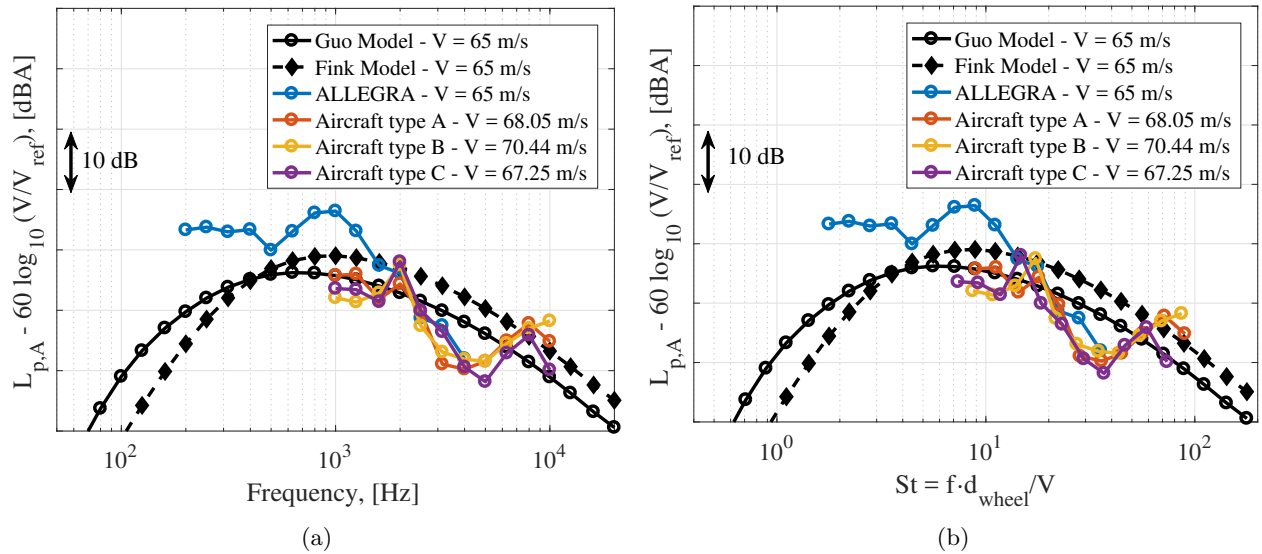


Figure 19: Spectra comparison of the NLG noise emissions in the flyover direction ($\theta \approx 90^\circ$, $\phi = 0^\circ$) between both noise prediction models, the ALLEGRA wind-tunnel experiments model with $V_{\text{ref}} = 65$ m/s and an example flyover measurement for each aircraft type: (a) Absolute frequencies. (b) Normalized frequencies with the Strouhal number ($St = f \cdot d_{\text{wheel}}/V$).

Fig. 19a is also displayed for reference. It can be observed that the noise contribution of the strut and bay door is slightly higher than that from the wheel, except for the one-third-octave band centered at 630 Hz, where the wheel presents considerably higher levels. Interestingly, the noise levels in the flyover direction are considerably lower than in the side direction for the whole frequency range, except between 800 Hz and 1200 Hz, where the aforementioned *hump* in the previous section causes an increase in the noise levels, even over the noise emissions in the side direction. Once again, no important tonal peaks were observed in the narrow-band spectra of the wind-tunnel experiments, which are not shown here for brevity reasons.

Figure 20b presents the comparison of the total noise emissions of the ALLEGRA NLG in the wind-tunnel tests in the side direction and the predictions of Fink’s and Guo’s models with $\phi = 90^\circ$. Once again, the wind-tunnel data present higher noise levels at low frequencies (below 400 Hz), which could be due to the higher background noise levels in the facility in that range. For frequencies higher than 400 Hz, the experimental data is bounded between the predictions of both noise prediction models, with a closer agreement to the results of Fink’s model in this case. For this emission direction, the wind-tunnel data show another hump (smaller than for the flyover direction) between 1 kHz and 2.5 kHz. None of the noise prediction models capture this trend.

The far-field acoustic spectra obtained by the *Side array 2* in the computational simulations are presented in Fig. 21, which shows the DNB results using the three dual-LPD approaches aforementioned and the propagated signal using the FW-H analogy. In this case, only the DNB_a spectrum shows a small peak at 2100 Hz (protruding about 5 dB over the broadband noise), whereas the other two DNB spectra present no important tonal peaks in the whole frequency range. The FW-H results contain several tonal peaks at about 1050 Hz and higher frequencies up to 2500 Hz. These peaks are not observed in the experimental data from the ALLEGRA wind-tunnel campaign.

Observing the source plots presented in Figs. 11 and 15, it could be proposed that the emissions of the main noise sources found between the NLG wheels, and around the axle, are perhaps shielded by the presence of the wheels themselves, which would explain the lack of tonal peaks in the spectra presented in Fig. 21. Once again, a more detailed numerical analysis is suggested.

VI. Conclusions

This paper compares microphone-array measurements on full-scale nose landing gears (NLG) for regional aircraft performed in flyover tests for three aircraft types under operational conditions, open-jet wind-tunnel

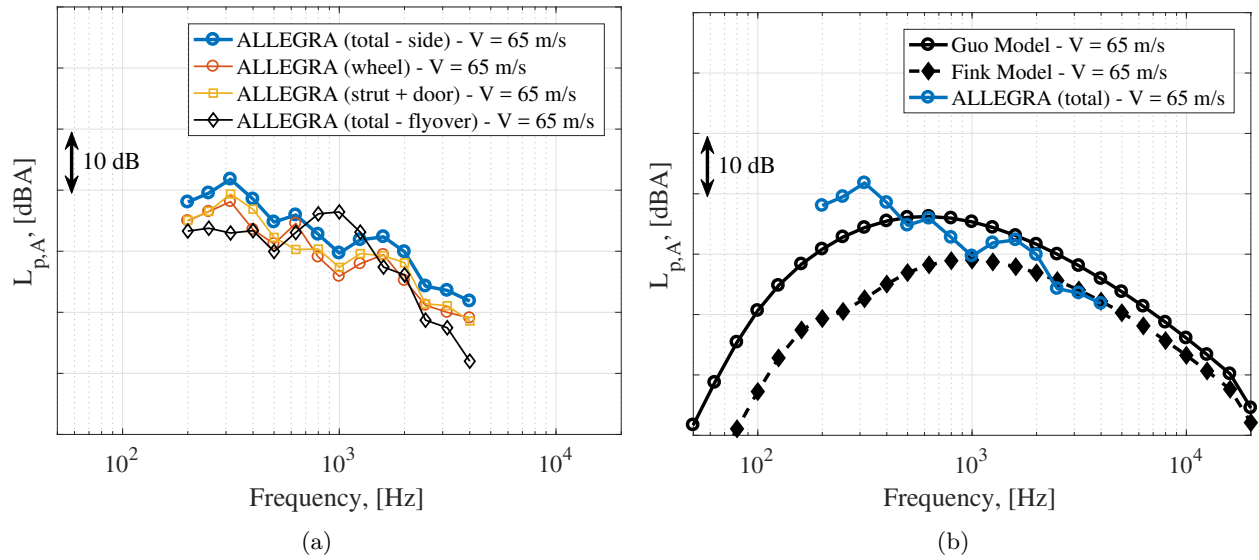


Figure 20: (a) Spectral breakdown for the noise emissions of the ALLEGRA NLG in the side direction ($\theta \approx 90^\circ$, $\phi \approx 90^\circ$) in the wind-tunnel tests. (b) Spectra comparison of the NLG noise emissions in the side direction between both noise prediction models and the ALLEGRA wind tunnel experiments model with $V_{\text{ref}} = 65$ m/s.

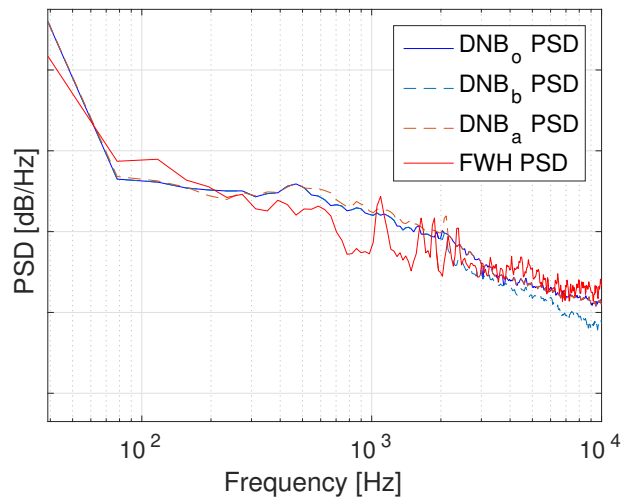


Figure 21: Far-field acoustic spectra obtained by the *Side array 2* in the computational simulations with DNB and the FW-H analogy. The grid step in the ordinate axis is 20 dB. The observer for the FW-H analogy is located at (2.826 m, 2 m, 1.8 m). Extracted from [27].

experiments and computational simulations. All the NLG presented similar geometries. Different emission directions were studied, but the flyover and side directions are analyzed in detail. The application of acoustic imaging methods on the microphone–array data allows for the estimation of the positions of the noise sources on the NLG. For the frequencies considered, the wind–tunnel tests and the computational simulations indicate that the main noise sources are located around the center of the wheel axle, followed by the main strut and bay doors.

The far–field sounds spectra obtained in the wind–tunnel experiments follow the expected 6th power law with the flow velocity. In addition, the wind–tunnel results show similar trends as those obtained for the flyover measurements, with the exception that the flyover results present strong tonal peaks around 2200 Hz, which are not observed in the wind–tunnel data. Such tones are considered to be of high annoyance for the population living near airports [71]. Removing these tones would cause overall noise reductions up to 2 dB in the frequency range examined. Similar tonal peaks at similar frequencies are also found in the outcome of the computational simulations. As proposed by previous research, it is suggested that these tones are caused by the presence of open cavities in the NLG system, since they do not seem to depend on the flow velocity. No important tonal peaks were observed in the side emission direction.

The obtained experimental results are compared with two widely–used airframe noise prediction models: Fink’s and Guo’s methods. The predictions of both methods present comparable trends as the experimental results, but do not consider the contributions of parasitic noise sources, such as cavities, in the calculations. Guo’s method provides a closer agreement in the flyover emission direction, whereas Fink’s method seems to offer a better match in the side emission direction.

Including cavity–noise estimations in the models would improve the noise predictions around airports. However, cavity noise is considerably difficult to predict since the intensity of the excitation of the cavity resonant mode depends on the velocity, turbulence levels and direction of the flow. Moreover, the tones due to cavity noise must be considered individually and cannot be represented in a convenient nondimensional form [3]. The use of cavity caps might be an effective and easy noise–reduction treatment [15] (keeping in mind practical and safety constraints). Other noise–reduction devices [41] can also help to reduce the LG emissions. In addition, due to the strong dependence between the noise emissions of the NLG (and most airframe noise sources, in general) and the flow velocity, an obvious recommendation would be to reduce the approach speed as much as possible, keeping in mind that the high–lift devices would generate more noise due to the additional lift requirement.

In conclusion, the importance of the use of phased microphone arrays in aeroacoustic experiments and simulations has been confirmed, as well as the advantages and limitations of different approaches in aeroacoustic studies. Hybrid studies as the one presented in this paper are, thus, of high interest, whenever possible. Furthermore, to ensure the validity of the results, full–scale tests under operational conditions are essential.

Future work is recommended, especially a more detailed computational study with higher resolution. Flyover measurements featuring larger microphone arrays and wind–tunnel tests with microphone arrays suitable for higher–frequency recordings are of high interest to extend the comparison over a larger frequency range.

Acknowledgments

The research leading to the ALLEGRA wind–tunnel results has received funding from the European Union’s Seventh Framework Programme (FP7/2007–2013) for the Clean Sky Joint Technology Initiative under grant agreements n° [308225] (ALLEGRA) and n° [620188] (ARTIC). Authors acknowledge all the partners that took part in the ALLEGRA and ARTIC projects.

The authors also acknowledge Hamza Bouchouireb from the Royal Institute of Technology (KTH) in Stockholm, Sweden, for his constructive discussions about the computational results.

References

- ¹ Ruijgrok, G., *Elements of aviation acoustics*, VSSD, Second ed., 2007, ISBN 1090–6562–155–5.
- ² Lighthill, M. J., “On sound generated aerodynamically, I: General theory,” *Proceedings of the Royal Society of London. Series A, Mathematical and Physical Sciences*, Vol. 211, No. 1107, 1952, pp. 564–587.

- ³ Heller, H. H. and Dobrzynski, W. M., “Sound Radiation from Aircraft Wheel–Well/Landing–Gear Configuration,” *Journal of Aircraft*, Vol. 14, No. 8, 1977, pp. 768–774.
- ⁴ Dobrzynski, W., “Almost 40 Years of Airframe Noise Research: What Did We Achieve?” *Journal of Aircraft*, Vol. 47, No. 2, March–April 2010, pp. 353–367.
- ⁵ “ACARE – Strategic Research & Innovation Agenda,” Tech. rep., 2012.
- ⁶ “Flightpath 2050 Europe’s Vision for Aviation,” Tech. rep., European Commission, 2012, ISBN 978–92–79–19724–6.
- ⁷ Neri, E., Kennedy, J., and Bennett, G., “Characterization of low noise technologies applied to a full scale fuselage mounted nose landing gear,” *Proceedings of the Internoise 2015/ASME NCAD Meeting, August 9 – 12 2015, San Francisco, CA, USA*, 2015, NCAD2015–5911.
- ⁸ Neri, E., Kennedy, J., and Bennett, G., “Aeroacoustic source separation on a full scale nose landing gear featuring combinations of low noise technologies,” *Proceedings of the Internoise 2015/ASME NCAD Meeting, August 9 – 12 2015, San Francisco, CA, USA*, 2015, NCAD2015–5912.
- ⁹ Kennedy, J., Neri, E., and Bennett, G., “The reduction of main landing gear noise,” *22nd AIAA/CEAS Aeroacoustics Conference. May 30 – June 1 2015. Lyon, France*, 2016, AIAA paper 2016–2900.
- ¹⁰ Michel, U. and Qiao, W., “Directivity of Landing–Gear Noise Based on Flyover Measurements,” *5th AIAA/CEAS Aeroacoustics Conference, May 10 – 12 1999, Bellevue, Greater Seattle, WA, USA*, 1998, AIAA paper 1999–1956.
- ¹¹ Bertsch, L., *Noise Prediction within Conceptual Aircraft Design*, Ph.D. thesis, DLR, 2013, DLR Forschungsbericht, ISRN DLR–FB–2013–20, ISSN 1434–8454.
- ¹² Piet, J., Molin, N., and Sandu, C., “Aircraft landing gear provided with at least one noise reducing means,” U.S. Patent number 8,256,702. 2012.
- ¹³ De Metz, F. C. and Farabee, T. M., “Laminar and Turbulent Shear Flow Induced Cavity Resonances,” *4th AIAA Aeroacoustics Conference. October 3 – 5 1977, Atlanta, Georgia, USA*, 1977, AIAA Paper 1977–1293.
- ¹⁴ Elder, S. A., Farabee, T. M., and De Metz, F. C., “Mechanisms of flow–excited cavity tones at low Mach number,” *Journal of the Acoustical Society of America*, Vol. 72, No. 2, August 1982, pp. 532–549.
- ¹⁵ Dobrzynski, W., Chow, L. C., Guion, P., and Shiells, D., “A European Study on Landing Gear Airframe Noise Sources,” *6th AIAA/CEAS Aeroacoustics Conference. June 12 – 14 2000, Lahaina HI, USA*, 2000, AIAA paper 2000–1971.
- ¹⁶ Dedoussi, I., Hynes, T., and Siller, H., “Investigating landing gear noise using fly–over data: the case of a Boeing 747–400,” *19th AIAA/CEAS Aeroacoustics Conference, May 27 – 29, 2013, Berlin, Germany*, 2013, AIAA paper 2013–2115.
- ¹⁷ Pott–Pollenske, M., Dobrzynski, W., Buchholz, H., Guérin, S., Saueressig, G., and Finke, U., “Airframe Noise Characteristics from Flyover Measurements and Predictions,” *12th AIAA/CEAS Aeroacoustics Conference. May 8 – 10 2006. Cambridge, Massachusetts, USA*, 2006, AIAA paper 2006–2567.
- ¹⁸ Fink, M. R., “Noise component method for airframe noise,” *4th AIAA Aeroacoustics Conference. October 3 – 5 1977, Atlanta, Georgia, USA*, 1977, AIAA Paper 1977–1271.
- ¹⁹ Merino–Martinez, R., Bertsch, L., Snellen, M., and Simons, D. G., “Analysis of landing gear noise during approach,” *22nd AIAA/CEAS Aeroacoustics Conference. May 30 – June 1 2016. Lyon, France*, 2016, AIAA paper 2016–2769.
- ²⁰ Merino–Martinez, R., Neri, E., Snellen, M., Kennedy, J., Simons, D., and Bennett, G., “Comparing flyover noise measurements to full–scale nose landing gear wind–tunnel experiments for regional aircraft,” *23rd AIAA/CEAS Aeroacoustics Conference. June 5 – 9 2017. Denver, Colorado, USA*, 2017, AIAA paper 2017–3006.

- ²¹ Dobrzynski, W. and Buchholz, H., “Full-scale noise testing on Airbus landing gears in the German Dutch Wind Tunnel,” *3rd AIAA/CEAS Aeroacoustics Conference. May 12 – 14 1997, Atlanta GA, USA, 1997*, AIAA paper 1997–1597.
- ²² Stoker, R., Guo, Y., Streett, C., and Burnside, N., “Airframe noise source locations of a 777 aircraft in flight and comparisons with past model-scale tests,” *9th AIAA/CEAS Aeroacoustics Conference. May 12 – 14 2003. Hilton Head, South California, USA, 2003*, AIAA paper 2003–3232.
- ²³ Takaishi, T., Ura, H., Nagai, K., Yokokawa, Y., Muruyama, M., Ito, Y., Sakai, R., Shoji, H., and Yamamoto, K., “Airframe noise measurements on JAXA Jet Flying Test Bed “Hisho” using a phased microphone array,” *International Journal of Aeroacoustics*, Vol. 16, No. 4–5, 2017, pp. 255–273, SAGE Publications Ltd. London, United Kingdom.
- ²⁴ Merino-Martinez, R., Snellen, M., and Simons, D. G., “Functional beamforming applied to imaging of flyover noise on landing aircraft,” *Journal of Aircraft*, Vol. 53, No. 6, November–December 2016, pp. 1830–1843.
- ²⁵ Simons, D. G., Snellen, M., Merino-Martinez, R., and Malgoezar, A. M. N., “Noise breakdown of landing aircraft using a microphone array and an airframe noise model,” *46th International Congress and Exposition of Noise Control Engineering, 27–30 August, 2017, Hong Kong, 2017*.
- ²⁶ Snellen, M., Merino-Martinez, R., and Simons, D. G., “Assessment of noise level variability on landing aircraft using a phased microphone array,” *Journal of Aircraft*, Vol. 54, No. 6, 2017, pp. 2173–2183.
- ²⁷ Bouchouireb, H., Pignier, N. J., O’Reilly, C., Boij, S., and Dahan, J., “Identification of noise sources on a realistic landing gear using numerical phased array methods applied to computational data,” *23rd AIAA/CEAS Aeroacoustics Conference. June 5 – 9 2017. Denver, Colorado, USA, 2017*, AIAA paper 2017–3019.
- ²⁸ Dahan, J. A., O’Reilly, C., and Efraimsson, G., “Numerical Investigation of a Realistic Nose Landing Gear,” *20th AIAA/CEAS Aeroacoustics Conference, June 16 – 20 2014, Atlanta, GA, USA, 2014*, AIAA paper 2014–2077.
- ²⁹ Dahan, J., Futrzynski, R., O’Reilly, C., and Efraimsson, G., “Aero-acoustic source analysis of landing gear noise via dynamic mode decomposition,” *21st International Congress on Sound and Vibration, July 13 – 17 2014, Beijing, China, Vol. 2, 2014*, pp. 1245–1252.
- ³⁰ Redonnet, S. and Bulté, J., “Landing Gear Noise Sources Identification through an Application of Array Methods to Experimental and Computational Data,” *22nd AIAA/CEAS Aeroacoustics Conference. May 30 – June 1 2016. Lyon, France, 2016*, AIAA paper 2016–2844.
- ³¹ Guo, Y., “Empirical Prediction of Aircraft Landing Gear Noise,” Tech. Rep. NASA TM–2005–213780, NASA, July 2005.
- ³² Guo, Y., “A Semi-Empirical Model for Aircraft Landing Gear Noise Prediction,” *12th AIAA/CEAS Aeroacoustics Conference. May 8 – 10 2006, Cambridge, Massachusetts, USA, 2006*, AIAA Paper 2006–2627.
- ³³ Guo, Y., “A component-based model for aircraft landing gear noise prediction,” *Journal of Sound and Vibration*, Vol. 312, 2008, pp. 801–820, Retracted from the journal.
- ³⁴ Burley, C. L., Brooks, T. F., Humphreys Jr., W. M., and W., R. J. J., “ANOPP Landing Gear Noise Prediction Comparisons to Model-Scale Data,” *13th AIAA/CEAS Aeroacoustics Conference (28th AIAA Aeroacoustics Conference), May 21 – 23 2017, Rome, Italy, 2007*, AIAA paper 2007–3459.
- ³⁵ Mueller, T., *Aeroacoustic Measurements*, Springer Science & Business Media, 2002, ISBN–978–3–642–07514–8.
- ³⁶ Merino-Martinez, R., Snellen, M., and Simons, D. G., “Functional Beamforming Applied to Full Scale Landing Aircraft,” *6th Berlin Beamforming Conference, February 29 – March 1 2016, Berlin, Germany, GFaI, e.V., Berlin, 2016*, BeBeC–2016–D12.

- ³⁷ Merino-Martinez, R., Snellen, M., and Simons, D. G., “Determination of Aircraft Noise Variability Using an Acoustic Camera,” *23rd International Congress on Sound and Vibration, July 10 – 14 2016, Athens, Greece*, 2016.
- ³⁸ Merino-Martinez, R., Sijtsma, P., Snellen, M., Ahlefeldt, T., Antoni, J., Bahr, C., Blacodon, D., Ernst, D., Finez, A., Funke, S., Geyer, T., Haxter, S., Herold, G., Huang, X., Humphreys, W., Leclère, Q., Malgoezar, A., Michel, U., Padois, T., Pereira, A., Picard, C., Sarradj, E., Siller, H., Simons, D. G., and Spehr, C., “Aircraft Noise Generation and Assessment: A review of acoustic imaging methods using phased microphone arrays,” *CEAS Aeronautical Journal*, 2017, Accepted for publication.
- ³⁹ Sijtsma, P., “Phased array beamforming applied to wind tunnel and fly-over tests,” Tech. Rep. NLR–TP–2010–549, National Aerospace Laboratory (NLR), Anthony Fokkerweg 2, 1059 CM Amsterdam, P.O. Box 90502, 1006 BM Amsterdam, The Netherlands, December 2010.
- ⁴⁰ Lockard, D. P., Humphreys, W. M., Khorrami, M. R., Fares, E., Casalino, D., and Ravetta, P. A., “Comparison of Computational and Experimental Microphone Array Results for an 18%–Scale Aircraft Model,” *International Journal of Aeroacoustics*, Vol. 16, No. 4–5, 2017, pp. 358–381, SAGE Publications Ltd. London, United Kingdom.
- ⁴¹ Neri, E., *Characterisation and Reduction of Aircraft Landing Gear Noise*, Ph.D. thesis, Trinity College Dublin, 2017.
- ⁴² Welch, P. D., “The Use of Fast Fourier Transform for the Estimation of Power Spectra: A Method Based on Time Averaging Over Short, Modified Periodograms,” *IEEE Transactions on Audio and Electroacoustics*, Vol. AU–15, No. 2, June 1967, pp. 70–73.
- ⁴³ Snellen, M., Merino-Martinez, R., and Simons, D. G., “Assessment of aircraft noise sources variability using an acoustic camera,” *5th CEAS Air & Space Conference. Challenges in European Aerospace. September 7 – 11 2015, Delft, Netherlands*, 2015.
- ⁴⁴ Howell, G. P., Bradley, M. A., McCormick, M. A., and Brown, J. D., “De–Dopplerization and acoustic imaging of aircraft flyover noise measurements,” *Journal of Sound and Vibration*, Vol. 105, No. 1, Feb 1986, pp. 151–167.
- ⁴⁵ Rossing, T. D., *Handbook of Acoustics*, Springer Science & Business Media, Second ed., 2007, ISBN 987–0–387–30446–5.
- ⁴⁶ Shur, M. L., Spalart, P. R., Strelets, M. K., and Travin, A. K., “A hybrid RANS–LES approach with delayed–DES and wall–modelled LES capabilities,” *International Journal of Heat and Fluid Flow*, Vol. 29, No. 6, 2008, pp. 1638–1649.
- ⁴⁷ Pignier, N. J., O’Reilly, C., and Boij, S., “Identifying equivalent sound sources from aeroacoustic simulations using a numerical phased array,” *Journal of Sound and Vibration*, Vol. 394, No. Supplement C, 2017, pp. 203–219.
- ⁴⁸ Ffowcs Williams, J. E. and Hawkings, D. L., “Sound generation by turbulence and surfaces in arbitrary motion,” *Philosophical Transactions of the Royal Society of London A – Mathematical, Physical and Engineering Sciences*, Vol. 264, No. 1151, May 1969.
- ⁴⁹ Amiet, R. K., “Refraction of sound by a shear layer,” *Journal of Sound and Vibration*, Vol. 58, No. 4, 1978, pp. 467–482.
- ⁵⁰ Merino-Martinez, R., Sijtsma, P., and Snellen, M., “Inverse Integration Method for Distributed Sound Sources,” *7th Berlin Beamforming Conference, March 5 – 6 2018, Berlin, Germany*, GFaI, e.V., Berlin, 2018, BeBeC–2018–S07.
- ⁵¹ Kennedy, J., Eret, P., Bennett, G., Sopranzetti, F., Chiarotti, P., Castellini, P., Finez, A., and Picard, C., “The application of advanced beamforming techniques for the noise characterization of installed counter rotating open rotor,” *19th AIAA/CEAS Aeroacoustics Conference. May 27 – 29 2013. Berlin, Germany*, 2013, AIAA paper 2013–2093.

- ⁵² Arce León, C., Merino-Martinez, R., Ragni, D., Avallone, F., and Snellen, M., “Boundary layer characterization and acoustic measurements of flow-aligned trailing edge serrations,” *Experiments in Fluids*, Vol. 57, No. 182, October 2016, pp. 1 – 22.
- ⁵³ Arce León, C., Merino-Martinez, R., Ragni, D., Avallone, F., Scarano, F., Pröbsting, S., Snellen, M., Simons, D. G., and Madsen, J., “Effect of trailing edge serration–flow misalignment on airfoil noise emission,” *Journal of Sound and Vibration*, Vol. 405, May 2017, pp. 19 – 33.
- ⁵⁴ Arce León, C., Merino-Martinez, R., Pröbsting, S., Ragni, D., and Avallone, F., “Acoustic Emissions of Semi-Permeable Trailing Edge Serrations,” *Acoustics Australia*, Vol. 1, 2017.
- ⁵⁵ Merino-Martinez, R., van der Velden, W. C. P., Avallone, F., and Ragni, D., “Acoustic measurements of a DU96–W–180 airfoil with flow-misaligned serrations at a high Reynolds number in a closed-section wind tunnel,” *7th International Meeting on Wind Turbine Noise, May 2 – 5 2017, Rotterdam, the Netherlands*, 2017.
- ⁵⁶ Sijtsma, P., Merino-Martinez, R., Malgoezar, A. M. N., and Snellen, M., “High-Resolution CLEAN-SC: Theory and Experimental Validation,” *International Journal of Aeroacoustics*, Vol. 16, No. 4–5, 2017, pp. 274–298, SAGE Publications Ltd. London, United Kingdom.
- ⁵⁷ Sijtsma, P., Merino-Martinez, R., Malgoezar, A. M. N., and Snellen, M., “High-Resolution CLEAN-SC: Theory and Experimental Validation,” *23rd AIAA/CEAS Aeroacoustics Conference. June 5 – 9 2017. Denver, Colorado, USA*, 2017, AIAA paper 2017–3841.
- ⁵⁸ Luesutthiviboon, S., Malgoezar, A., Snellen, M., Sijtsma, P., and Simons, D. G., “Improving Source Discrimination Performance by Using an Optimized Acoustic Array and Adaptive High-Resolution CLEAN-SC Beamforming,” *7th Berlin Beamforming Conference, March 5 – 6 2018, Berlin, Germany*, GfA, e.V., Berlin, 2018, BeBeC–2018–D07.
- ⁵⁹ Dougherty, R. P., “Functional Beamforming,” *5th Berlin Beamforming Conference, February 19 – 20 2014, Berlin, Germany*, GfA, e.V., Berlin, 2014.
- ⁶⁰ Dougherty, R. P., “Functional Beamforming for Aeroacoustic Source Distributions,” *20th AIAA/CEAS Aeroacoustics Conference. June 16 – 20 2014. Atlanta GA, USA*, 2014, AIAA paper 2014–3066.
- ⁶¹ Camier, C., Padois, T., Provencher, J., Gauthier, P.-A., Berry, A., Blais, J. F., Patenaude-Dufour, M., and Lapointe, R., “Fly-over source localization on civil aircraft,” *19th AIAA/CEAS Aeroacoustics Conference. May 27 – 29 2013. Berlin, Germany*, 2013, AIAA paper 2013–2261.
- ⁶² Dougherty, R. P., “Cross Spectral Matrix Diagonal Optimization,” *6th Berlin Beamforming Conference, February 29 – March 1, 2016, Berlin, Germany*, GfA, e.V., Berlin, 2016.
- ⁶³ Dougherty, R. P., Ramachandran, R. C., and Raman, G., “Deconvolution of Sources in Aeroacoustic Images from Phased Microphone Arrays Using Linear Programming,” *19th AIAA/CEAS Aeroacoustics Conference, May 27 – 29 2013, Berlin, Germany*, 2013, AIAA paper 2013–2210.
- ⁶⁴ Brooks, T. F. and Humphreys, W. M., “A Deconvolution Approach for the Mapping of Acoustic Sources (DAMAS) determined from phased microphone arrays,” *Journal of Sound and Vibration*, Vol. 294, No. 4–5, 2006, pp. 856–879.
- ⁶⁵ Zorumski, W. E., “Aircraft Noise Prediction Program – Theoretical Manual – Part 1,” Tech. Rep. NASA Technical Memorandum 83199, NASA Technical Memorandum 83199, 1982.
- ⁶⁶ Zorumski, W. E., “Aircraft Noise Prediction Program – Theoretical Manual – Part 2,” Tech. Rep. NASA Technical Memorandum 83199, NASA Technical Memorandum 83199, 1982.
- ⁶⁷ Curle, N., “The influence of solid boundaries upon aerodynamic sound,” *Proceedings of Royal Society of London A*, Vol. 231, No. 1187, September 1955, pp. 505–514.
- ⁶⁸ Guo, Y., Yamamoto, K. J., and Stoker, R. W., “Experimental Study on Aircraft Landing Gear Noise,” *Journal of Aircraft*, Vol. 43, No. 2, November–December 2006, pp. 306–317.

- ⁶⁹ Aures, W., “Procedure for calculating the sensory euphony of arbitrary sound signal,” *Acustica*, Vol. 59, No. 2, 1985, pp. 130–141.
- ⁷⁰ Sahai, A. K. and Stumpf, E., “Incorporating and Minimizing Aircraft Noise Annoyance during Conceptual Aircraft Design,” *20th AIAA/CEAS Aeroacoustics Conference, June 16 – 20 2014, Atlanta, GA, USA*, 2014, AIAA paper 2014–2078.
- ⁷¹ Sahai, A. K., *Consideration of Aircraft Noise Annoyance during Conceptual Aircraft Design*, Ph.D. thesis, Rheinisch–Westfälische Technische Hochschule Aachen, 2016.